TU Delft

Delft University of Technology

Document Version
Final published version

Licence
CC BY

Citation (APA)
Dijks, J., De Jong, S., Menicucci, A., Akay, I., & Donkers, N. (2026). Comparative Investigation of Radiation-Driven Failure Mechanisms in Photonic-Electronic Optical Communication Terminals Across Earth Orbits. *IEEE Access*, *14*, 68864-68883. https://doi.org/10.1109/ACCESS.2026.3690234

Important note
To cite this publication, please use the final published version (if applicable).
Please check the document version above.

Copyright
In case the licence states "Dutch Copyright Act (Article 25fa)", this publication was made available Green Open Access via the TU Delft Institutional Repository pursuant to Dutch Copyright Act (Article 25fa, the Taverne amendment). This provision does not affect copyright ownership.
Unless copyright is transferred by contract or statute, it remains with the copyright holder.

Sharing and reuse
Other than for strictly personal use, it is not permitted to download, forward or distribute the text or part of it, without the consent of the author(s) and/or copyright holder(s), unless the work is under an open content license such as Creative Commons.

Takedown policy
Please contact us and provide details if you believe this document breaches copyrights.
We will remove access to the work immediately and investigate your claim.

This work is downloaded from Delft University of Technology.

IEEE Access
Multidisciplinary : Rapid Review : Open Access Journal

Received 2 April 2026, accepted 30 April 2026, date of publication 4 May 2026, date of current version 8 May 2026.

Digital Object Identifier 10.1109/ACCESS.2026.3690234

RESEARCH ARTICLE

Comparative Investigation of Radiation-Driven Failure Mechanisms in Photonic–Electronic Optical Communication Terminals Across Earth Orbits

JASPER DIJKS[1,2], SYBREN DE JONG[1], ALESSANDRA MENICUCCI[2], IKLIM AKAY[2], AND NIELS DONKERS[3]

[1]Division of Aerospace Systems, Royal NLR, 1059 CM Amsterdam, The Netherlands
[2]Department of Space Systems Engineering, TU Delft, 2629 HS Delft, The Netherlands
[3]FSO Instruments, 2628 XJ Delft, The Netherlands

Corresponding author: Jasper Dijks (jasper.dijks@nlr.nl)

This work was supported by the Dutch National Growth Fund through the NXTGEN HIGHTECH Program.

ABSTRACT Optical Communication Terminals (OCTs) integrate photonic and electronic technologies to enable high-speed, secure, and interference-free space communication. Deployment across multiple orbital regimes exposes these heterogeneous systems to diverse radiation environments, each presenting distinct failure mechanisms that challenge conventional Radiation Hardness Assurance (RHA) approaches, particularly for cost-constrained Small Satellite (SmallSat)-class missions where economic feasibility must be balanced against radiation hardness requirements. This paper presents a multi-orbit radiation effects investigation for photonic-electronic architectures by characterizing environment-specific vulnerabilities and failure modes across Sun-Synchronous Orbit (SSO), Low Earth Orbit (LEO), and Middle Earth Orbit (MEO). SPENVISbased environment analysis shows that SSO presents a mild radiation environment with Total Ionizing Dose (TID) below 1 krad(Silicon (Si)) per year at 4 mm Aluminium (Al) shielding and low charged particle flux. LEO is dominated by proton-induced Single Event Effects (SEEs) with moderate TID, and MEO exhibits TID exceeding 30 krad(Si) per year at the same shielding level, together with relatively higher heavy-ion fluxes that drive SEE rates. Technology-level analysis reveals fundamental differences between photonic and electronic subsystems. Photonics exhibits predominantly parametric degradation that can be mitigated through margin allocation, whereas electronics remains susceptible to discrete, stochastic failure modes requiring active mitigation. These findings motivate reconfigurable architectures leveraging Field Programmable Gate Arrays (FPGAs), radiation-tolerant photonic subsystems,Wide-Bandgap (WBG) power semiconductors, and emerging Non-Volatile Memories (NVMs) to enable component-level commonality across orbital regimes. Additionally, photonic devices require parametric end-of-life characterization with explicit translation to link budget margins, while electronic systems require mission-tailored mitigation strategies and system-level testing.

INDEX TERMS Optical communication terminals, photonics, electronics, radiation effects, radiation hardness assurance.

I. INTRODUCTION

Spaceborne Optical Communication Terminals (OCTs) enable secure, high-bandwidth, and interference-free data transmission and are increasingly central to emerging Small Satellite (SmallSat)-class (typically <1200 kg) constellations. Compared to traditional Radio Frequency (RF) systems, OCT architectures deliver superior performance at significantly lower Size, Weight, Power and Cost (SWaP-C), relying on tightly integrated photonic, digital, and

The associate editor coordinating the review of this manuscript and approving it for publication was Sukhdev Roy.

© 2026 The Authors. This work is licensed under a Creative Commons Attribution 4.0 License.
For more information, see https://creativecommons.org/licenses/by/4.0/

mixed-signal components. Anticipated deployments across Sun-Synchronous Orbit (SSO), Low Earth Orbit (LEO), and Middle Earth Orbit (MEO) expose these systems to various radiation environments, where Total Ionizing Dose (TID), Displacement Damage (DD), and Single Event Effects (SEEs) pose significant reliability risks over multi-year mission lifetimes. Radiation effects and Radiation Hardness Assurance (RHA) practices for electronic systems have been extensively studied over several decades [1], [2], [3], [4], [5], yet continued device scaling and increasing reliance on Commercial Off-The-Shelf (COTS) components present persistent challenges [6], [7], [8]. Higher integration density, accelerated obsolescence cycles, and limited fabrication transparency complicate both the prediction of radiation response [9] and the implementation of RHA [10].

Literature consistently identifies radiation effects in space optoelectronic systems as an active and evolving area of research [11], [12], [13], [14]. A dedicated review of Photonic Integrated Circuits (PICs) for optical satellite links surveys the state of photonic device technologies and discusses the potential impact of radiation on integrated photonic performance [11]. A complementary survey of radiation-induced degradation in optoelectronic space systems broadens the perspective to include electronic–optical interactions and qualification challenges in all technologies [13]. Another experimental study notes that, despite numerous proposals for System on Chip (SoC) optical integration in space avionics, the literature on the impacts of space radiation on nanoscale photonic devices remains limited [12]. This highlights challenges arising from poorly constrained radiation spectra and significant device-to-device variability, which complicate identification of dominant physical degradation and failure mechanisms. As a result, while substantial knowledge exists on radiation effects in individual components, there remains limited system-level understanding of how these effects translate to photonic-electronic OCT architectures deployed across different orbital regimes. This complicates the reuse and scaling of OCTs designs across missions, increases reliance on orbit-specific redesign and requalification, and obscures where radiation effects are comparable versus where distinct mitigation strategies are required. The objective of this work is therefore not to replace existing radiation effects studies, but to synthesize and contextualize them into a comparative, design-oriented analysis for photonic-electronic systems across multiple orbital regimes.

This paper addresses this need through a radiation effects analysis tailored to OCTs operating across multiple orbital regimes. While the radiation environment analysis employs established tools and models, the novelty lies in the systematic correlation of environment-specific threats with technology-specific failure modes across heterogeneous photonic–electronic architectures, an analysis not previously available for OCTs spanning multiple orbits. The principal contributions are: (1) a technology-focused vulnerability analysis of key photonic and electronic OCT components; (2) a quantitative comparison of radiation environments across SSO, LEO, and MEO, identifying regime-specific dominant threats; and (3) comparative correlation of orbital radiation spectra with component-level sensitivities. To enable a consistent comparison of radiation effects across orbital regimes and photonic–electronic technologies, the fundamental particle interaction and energy deposition mechanisms underlying radiation-induced failures are established in Section II. Subsequently, Section III examines OCT components and their sensitivities. Section IV presents the multi-orbit radiation environment analysis, including dose accumulation. Section V synthesizes the dominant radiation-induced failure modes and their implications for OCT architectures and validation. Section VI concludes and summarizes the work.

II. RADIATION MECHANISMS

A structured comparison of radiation effects across orbital regimes requires a common physical basis. This section therefore reviews the fundamental particle interaction and energy deposition mechanisms that give rise to cumulative and transient radiation effects in spacecraft avionics [3]. While these mechanisms are traditionally discussed in the context of microelectronics, the same interaction physics governs radiation-induced degradation in photonic devices. The interaction mechanisms and resulting damage depend on particle type, energy, and charge state [15], [16], [17].

A. PARTICLE INTERACTIONS

Radiation damage in spacecraft avionics originates from energy deposition when incident particles interact with materials. The amount and spatial distribution of deposited energy determine whether effects manifest as cumulative degradation or instantaneous effects. Space radiation interacts with matter through three primary pathways: photon interactions (photoelectric effect, compton scattering, pair production), charged particle interactions (bremsstrahlung, ionization, excitation), and nuclear interactions (absorption, fission, (in)elastic scattering), as illustrated in Figure 1. Photon and charged particle interactions deposit energy primarily through electronic excitation and ionization, generating electron–hole pairs central to radiation effects in semiconductors. Nuclear interactions transfer energy through atomic displacements and recoil, producing lattice defects. All mechanisms may contribute either directly or through secondary particle generation. Detailed information on interaction cross-sections and energy-dependent behavior is available in standard [18].

B. ENERGY DEPOSITION

The interactions described above deposit energy in materials through two distinct pathways: electronic energy loss through ionization and excitation, and nuclear energy loss with atomic displacements. These mechanisms underpin the metrics used to quantify radiation effects in spacecraft systems.

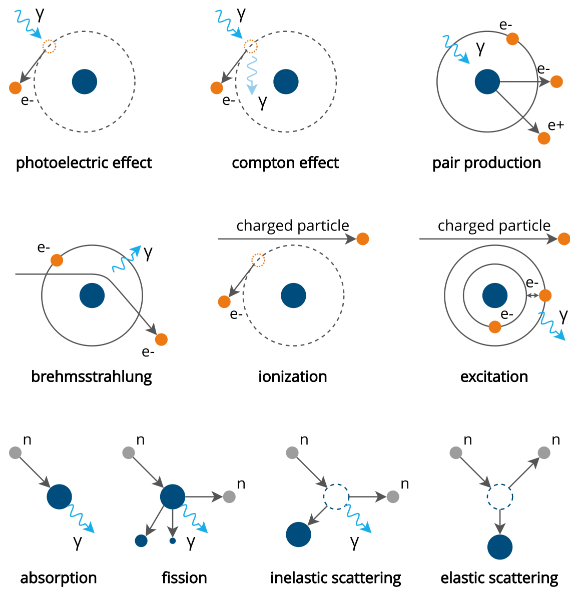

FIGURE 1. Illustration of primary radiation interaction mechanisms with matter: photon interactions showing photoelectric effect, compton scattering, and pair production; charged particle interactions depicting bremsstrahlung, ionization, and excitation; nuclear interactions showing absorption, fission, and (in)elastic scattering. Adapted from [19].

1) ELECTRONIC ENERGY LOSS

When charged particles traverse matter, energy loss occurs through stochastic interactions with electrons. The mean stopping power in MeV cm^{-1} is described by the Bethe equation [18]:

$$-\left\langle \frac{dE}{dx} \right\rangle = K \frac{\rho Z}{A} \frac{z^2}{\beta^2} \left(\frac{1}{2} \ln \frac{2m_e c^2 \beta^2 \gamma^2 W_{\max}}{I^2} - \beta^2 - \frac{\delta(\beta\gamma)}{2} \right), \quad (1)$$

where $K = 4\pi N_A \alpha^2 \hbar^2 / m_e$ contains fundamental constants, Z and A are the atomic number and atomic mass of the target material, ρ the density of the target material, z is the projectile charge number, $\beta = v/c$, and $\gamma = 1/\sqrt{1-\beta^2}$, and I is the mean excitation energy. The equation contains the density-effect correction term $\delta(\beta\gamma)$, important at high γ. $W_{\max}$ is the maximum energy transfer to a free electron:

$$W_{\max} = \frac{2m_e c^2 \beta^2 \gamma^2}{1 + 2\gamma m_e/M + (m_e/M)^2}, \quad (2)$$

where M is the incident particle mass and m_e is the electron mass. Key dependencies in Equation (1) include the $1/\beta^2$ term producing the Bragg peak at low energies, and the linear scaling with target density and projectile charge number. The equation describes the mean energy loss, actual energy deposition is stochastic and varies with material thickness and particle energy.

Linear Energy Transfer (LET) quantifies the ionizing energy deposited by electronic interactions per unit mass thickness and is derived from the stopping power in Equation (1) [3]:

$$\text{LET} = -\frac{1}{\rho} \frac{dE}{dx}. \quad (3)$$

LET is expressed in units of MeV cm^2 g^{-1} and is a primary metric for characterizing SEEs in space systems, but also foundational for TID effects.

2) NUCLEAR ENERGY LOSS

In contrast to electronic interactions, nuclear energy loss occurs when particles interact with atomic nuclei through elastic and inelastic collisions, displacing lattice atoms rather than creating electron-hole pairs. Nuclear stopping dominates at sufficiently low particle energies where electronic interactions become inefficient. To account for these interactions, higher-order corrections to the bracketed term in Equation (1) are required [18].

The Non-Ionizing Energy Loss (NIEL) can be determined using an analytic expression that sums these elastic and inelastic contributions [20]:

$$\text{NIEL} = \frac{N_A}{A} \left(\sigma_e W_e + \sigma_i W_i \right), \quad (4)$$

where σ_e and σ_i are the total elastic and inelastic nuclear interaction cross sections, and W_e and W_i are average recoil energies corrected for ionization loss. Like LET in Equation (3), NIEL is expressed in MeV cm^2 g^{-1} and characterizes DD effects.

C. RADIATION EFFECTS

The particle interactions and energy deposition mechanisms described above give rise to radiation effects in spacecraft systems through both cumulative and transient processes. During space missions, radiation-induced effects have caused performance drift, functional anomalies, and permanent failures across a wide range of technologies [21]. These effects are commonly categorized as cumulative damage driven by TID and DD, or as transient effects arising from SEEs. Their severity and manifestation depend on the incident particle spectrum, the shielding configuration, the material composition, the system-level architecture, and mitigation strategies. Because radiation-induced effects originate at the material and device levels but ultimately propagate to system-level behavior, a physics-based understanding is essential for assessing heterogeneous spacecraft subsystems. Together, TID, DD, and SEEs establish the link between the fundamental interaction physics discussed before and the technology-specific vulnerabilities examined in the subsequent section.

1) TOTAL IONIZING DOSE

TID represents the cumulative ionizing energy deposited in a material over time and is commonly expressed in gray (Gy) or rad (1 rad is equal to 0.01 Gy). For a monoenergetic particle fluence, the accumulated dose can be approximated as

$$\text{TID} = e\,\Phi \cdot \text{LET} \cdot 10^{-9}, \quad (5)$$

where e is the elementary charge and Φ is the particle fluence in cm^{-2}. The factor 10^{-9} accounts for unit conversion from MeV g^{-1} to J kg^{-1}. In realistic space radiation environments, TID accumulates from contributions across a broad particle energy spectrum and is obtained by integrating or summing Equation (5) over all relevant particle species and energies. The fluence Φ is determined by integrating the time-dependent particle flux $\phi(t)$, expressed in cm^{-2} s^{-1}, over the mission duration.

Ionizing radiation deposits energy primarily through the generation of electron-hole pairs in insulating and semiconducting materials. The subsequent transport, trapping, and recombination of these carriers modify local electric fields and material properties. A representative example is the response of Metal–Oxide–Semiconductor (MOS) structures, where ionizing radiation generates electron-hole pairs in gate oxides. Electrons rapidly escape due to their high mobility, while holes may become trapped within the oxide or at material interfaces, leading to threshold voltage shifts, increased leakage currents, and long-term parametric drift. Partial recombination and thermally activated annealing can produce time-dependent recovery effects. Although continued device scaling and reduced oxide thickness have mitigated some classical TID sensitivities, modern technologies exhibit new effect mechanisms, including enhanced leakage and field-dependent effects [2], [22]. Similar ionization-driven processes affect photonic materials, where radiation-induced charge trapping in oxides and interfaces, together with bulk defect formation, alters refractive index, increases optical absorption via mid-gap states, and degrades carrier lifetime through non-radiative recombination [23], [24].

2) DISPLACEMENT DAMAGE

DD arises from non-ionizing energy deposition associated with elastic and inelastic nuclear interactions that displace atoms from their lattice sites, forming vacancies, interstitials, and complex defect clusters. Unlike TID, which accumulates through electronic energy loss, DD accumulates through nuclear energy loss quantified by NIEL. The corresponding Total Non-Ionizing Dose (TNID) is obtained by convolving NIEL with the particle fluence, analogous to the TID calculation in Equation (5). In practice, TNID is often expressed in units of MeV g^{-1} rather than Gy or rad, yielding

$$\mathrm{TNID} = e\,\Phi \cdot \mathrm{NIEL}. \tag{6}$$

Displaced lattice atoms introduce defect states within the band gap that alter charge transport, recombination dynamics, and optical properties [20]. Subsequent annealing processes, which depend on temperature and carrier injection conditions, may partially heal or further evolve these defects over time, making DD-induced degradation strongly dependent on particle energy, material composition, and post-irradiation history. In electronic devices, these effects commonly manifest as increased leakage current, reduced carrier mobility, and gain degradation. In photonic devices, lattice damage can induce volume compaction or expansion, modify the refractive index through bulk defect formation, and degrade modulation efficiency [24], [25]. Because both DD and TID alter defect populations and charge transport, their effects can interact synergistically in complex device structures.

3) SINGLE EVENT EFFECTS

In contrast to cumulative degradation, SEEs are transient phenomena caused by individual particle strikes that deposit sufficient charge within a sensitive volume to disrupt normal operation. SEEs occur when the particle LET exceeds a technology- and geometry-dependent critical threshold. Charge deposition may result from direct ionization by heavy ions or from indirect ionization when protons or neutrons generate high-LET secondary particles through nuclear reactions. The deposited charge is collected through drift and diffusion processes, producing localized current transients that can alter circuit or device states [1].

SEEs are commonly classified as non-destructive or potentially destructive. Physically non-destructive effects include Single Event Upsets (SEUs), in which the state of a memory element or logic node is altered, and Multiple-Bit Upsets (MBUs), where a single event affects multiple storage elements. Single Event Functional Interrupts (SEFIs) correspond to more complex disruptions in which a particle strike places an integrated circuit into a temporary fault state requiring recovery. Single Event Transients (SETs) manifest as short-duration voltage or current perturbations in combinational logic and analog circuits, and can potentially cause any of the aforementioned transient effects. [26]. Potentially destructive effects include Single Event Latch-ups (SELs), which activate parasitic current paths, Single Event Gate Ruptures (SEGRs), which cause localized dielectric breakdown, and Single Event Burnouts (SEBs), which induce thermal runaway in power devices. Without appropriate mitigation, these events can lead to permanent functional loss [27].

Photonic devices can also experience SEEs through mechanisms that differ fundamentally from those in electronic circuits. One mechanism occurs when an energetic particle generates a dense cloud of electron-hole pairs within or near an optical waveguide. The resulting increase in free-carrier density leads to transient optical attenuation through free-carrier absorption, inducing optical power losses [28]. This is also described by the term Optical Single Event Transient (OSET), defined as a radiation-induced transient perturbation of optical power within an integrated photonic component [29].

III. OCT TECHNOLOGIES

OCT avionics rely on tightly coupled electronic and photonic technologies whose reliability is constrained by their response to the space radiation environment. This section reviews the space avionics technologies most relevant to OCTs from a radiation-effects perspective. The objective is to identify dominant radiation-induced failure mechanisms,

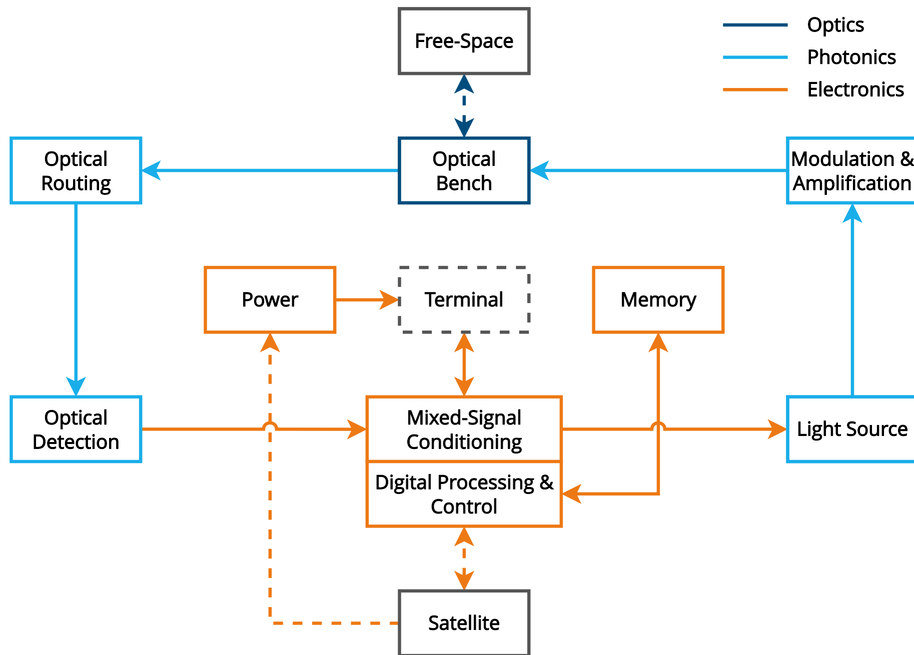

FIGURE 2. Functional block diagram of representative OCT architecture showing electronic and photonic subsystem interfaces.

their physical origins, and their system-level manifestations, enabling direct correlation with the orbital radiation environments analyzed in subsequent sections. Figure 2 provides a functional overview of the key electronic and photonic building blocks in a representative OCT. Bulk optical components are outside the scope of this section.

A. ELECTRONICS

Electronic subsystems form the control, processing, data handling, storage, and power backbone of OCTs and are primary drivers of radiation-induced functional disruption. This subsection reviews the electronic technologies most relevant to OCT avionics. The synthesis emphasizes dominant radiation-induced failure mechanisms, to support correlation with the orbital radiation environments and assurance strategies developed in subsequent sections.

1) DIGITAL PROCESSING AND CONTROL

Digital processing elements provide both control- and data-plane functionality in OCT avionics. Control logic governs terminal configuration, Pointing, Acquisition, and Tracking (PAT), and fault management, and therefore prioritizes high availability and deterministic behavior. Data logic supports high-throughput signal processing, modulation and demodulation, encoding, Error Detection and Correction (EDAC), and payload data handling, where transient errors can often be tolerated or corrected at higher abstraction levels. In SmallSat-class space avionics, which represent the primary target platform for OCTs, these functions are predominantly implemented using Field Programmable Gate Arrays (FPGAs) and Microcontroller Units (MCUs), with SoC devices and Digital Signal Processors (DSP) used more selectively, including in hybrid processing architectures [30]. These distinct roles lead to different sensitivity profiles and mitigation requirements under radiation exposure.

FPGAs play a critical role in space avionics because of their architectural flexibility and their ability to integrate both control- and data-plane functions into a single device. Radiation-induced effects in FPGAs primarily arise from cumulative ionizing damage and SEEs. The dominant failure mechanisms depend heavily on the underlying memory technology and internal architecture [31], [32]. Across all FPGA technologies, SETs can occur in user flip-flops, leading to upsets in the user logic. The effect of radiation depends on the configuration memory technology used. In Static Random Access Memory (SRAM)-based FPGAs, the configuration memory itself is also highly susceptible to SEUs, making these devices particularly sensitive to radiation effects. Block RAM (BRAM) is similarly vulnerable to SEUs. When SETs occur or propagate to the FPGA state management circuitry, SEFIs can occur, though this represents a smaller area and is therefore less sensitive than configuration memory [33], [34]. Flash-based FPGAs reduce sensitivity to memory SEEs but face distinct challenges due to TID, particularly in floating-gate circuitry, which limits their use in high-dose missions [35]. For both technologies, TID can also cause propagation delays [22]. SELs are also possible in both technologies, though their occurrence often depends on particle energy and the bias voltage in the I/O banks. In advanced technology nodes, charge sharing in routing and configuration resources further increases the likelihood of MBUs. The reliability of FPGAs in OCTs is generally

determined by the integrity of their configuration state rather than transient data-path errors. This highlights the need for mitigation strategies such as configuration scrubbing, selective or full Triple Modular Redundancy (TMR), and system-level error detection and recovery mechanisms [33], [36].

Fixed-function processors, such as general-purpose MCUs, provide an alternative to FPGAs for OCT tasks dominated by sequential control and software-defined functionality. Radiation-induced faults in such processors primarily manifest as transient state corruption, control-flow errors, or SEFIs caused by SEUs and SETs in registers, on-chip memories, and peripheral control logic. Experimental studies on low-power COTS processors show that, while destructive events such as SELs are often rare or limited in severity, SEFIs leading to processor resets, hangs, or peripheral malfunction can dominate observed failure rates, directly impacting system availability rather than data integrity [37], [38]. Flash memory in commercial MCUs exhibits increasing susceptibility to corruption and loss of writability at elevated TID levels, with some devices showing significant degradation beyond 200 krad(Silicon (Si)). Configuration-dependent sensitivity further complicates reliability assessment, as Central Processing Unit (CPU) SEE cross-sections can vary by an order of magnitude based on cache usage and peripheral settings. As a result, processor suitability for OCT avionics is largely determined by recoverability and observability under radiation exposure, motivating mitigation strategies based on watchdog timers and external reset handling for soft error recovery, selective use of Error Correcting Code (ECC) where available, and task-level redundancy rather than fine-grained hardware hardening [38].

2) MIXED-SIGNAL CONDITIONING

Mixed-signal conditioning circuits interface the digital processing chain with physical signals in OCT avionics, supporting functions such as sensor readout, bias generation, monitoring, and actuator drive. These circuits combine precision analog front-ends with embedded digital control and configuration logic. Their radiation response is therefore governed by the combined effects of cumulative degradation and destructive transient events in analog devices and additional non-destructive SEEs affecting associated digital elements, often leading to subtle and difficult-to-detect system-level failure modes.

In conventional Complementary MOS (CMOS)-based mixed-signal circuits, TID effects dominate long-term degradation through charge trapping in gate and isolation oxides and the formation of interface states. This results in threshold voltage shifts, leakage current increase, transconductance reduction, and excess low-frequency noise directly degrade gain, offset, linearity, and Signal-to-Noise Ratio (SNR) [39]. While aggressively scaled gate oxides may exhibit improved tolerance, thicker isolation oxides and I/O devices remain vulnerable, making mixed-signal blocks particularly susceptible to performance loss under accumulated dose [5].

At the system level, design diversity redundancy can partially mitigate these effects. Mixed-signal diversity TMR has been shown to improve resilience against TID-induced degradation by avoiding common-mode failures inherent to identical implementations. Experimental results indicate that performance degradation in individual channels, such as nonlinearity growth in data converters, does not necessarily propagate to system-level failure when architectural and temporal diversity are employed [40]. Such techniques are typically applied at the functional block level, as fine-grained redundancy within mixed-signal circuitry is often impractical.

Circuit-level mitigation strategies differ fundamentally between digital and analog domains. While digital storage elements can leverage hardened structures such as Dual Interlocked Cell (DICE) latches, analogous hardening in analog circuitry is less straightforward. Radiation-tolerant analog design techniques include current-mode operation, elimination of sensitive reference current sources, increased capacitance, and bias point optimization to reduce susceptibility to parameter shifts [5], [41]. These measures can improve tolerance to cumulative damage but typically impose trade-offs in power consumption, bandwidth, or noise performance.

SEEs can further disrupt analog circuits through transient perturbations in bias networks or embedded digital logic, leading to temporary misconfiguration or SEFIs. Alternative semiconductor technologies such as Silicon Germanium (SiGe) bipolar CMOS have demonstrated enhanced tolerance to TID and reduced susceptibility to SELs due to their heterojunction device physics. However, SEUs in associated CMOS logic remain possible, and the impact of SETs on high-speed SiGe analog signal paths remains an active area of investigation [42], [43].

In addition to CMOS-based implementations, Gallium Arsenide (GaAs) technologies have been historically employed in analog and RF conditioning circuits due to their high electron mobility and resistance to SELs. Radiation studies indicate comparatively strong tolerance to TID, with dominant degradation instead driven by DD, leading to gradual gain reduction and increased noise rather than abrupt functional failure [44]. While Si-based technology integration is usually favored, GaAs remains relevant for high frequency analog front-ends where predictable parametric degradation is preferred over SEEs disruption.

3) MEMORY

Memory technologies used in OCT avionics can include volatile memories, such as Dynamic RAM (DRAM) and SRAM, and Non-Volatile Memories (NVMs) based on flash and emerging memory technologies. Volatile memories offer low latency and high endurance but require continuous power,

while flash provides non-volatility at the cost of increased write latency and sensitivity to cumulative radiation damage. In space environments, charge-based memories are susceptible to TID, SEUs, MBUs, and SEFIs, necessitating the use of EDAC, redundancy, and periodic memory scrubbing to ensure reliable operation [45].

Flash memory devices are particularly vulnerable to TID due to degradation of charge pumps and floating-gate structures, affecting write and erase functionality. Both NOR and NAND architectures exhibit comparable radiation sensitivity, with no clear inherent advantage in radiation tolerance [46]. As a result, flash memory reliability in OCTs is typically governed by peripheral circuitry and system level mitigation rather than intrinsic cell robustness.

Emerging NVM technologies, including Spin-Transfer Torque Magnetic RAM (STT-MRAM), Resistive RAM (ReRAM), Conductive-Bridge RAM (CBRAM), Phase-Change RAM (PCRAM), and Ferroelectric RAM (FeRAM), replace charge-based storage with magnetic, resistive, or phase-change mechanisms and therefore exhibit improved tolerance to cumulative ionizing radiation [47]. While the memory cells themselves show strong resilience to TID, dynamic operation remains susceptible to SEEs, primarily through associated control and interface logic rather than the storage elements [48]. Radiation response in PCRAM and FeRAM further depends on material stability, with heavy-ion exposure inducing defect formation or bond reconfiguration processes that can affect long-term reliability [49].

4) POWER

Power electronics support power conversion, regulation, and distribution in Direct Current (DC)-DC converters, linear regulators, and driver circuitry. In conventional Si-based power devices, cumulative radiation damage primarily manifests through TID and DD. TID in power MOS Field-Effect Transistors (MOSFETs) leads to threshold voltage shifts, increased on-resistance, elevated leakage currents, and reduced breakdown margins, while bipolar devices exhibit gain degradation due to increased electron-hole recombination in the base-emitter junction. In associated control circuitry, degradation in CMOS logic can reduce Pulse Width Modulation (PWM) accuracy and switching stability. DD further impacts opto-couplers through reduced current transfer ratio [50].

SEEs represent a dominant risk for power electronics due to their potential for catastrophic failure. Heavy-ion interactions can trigger SEB and SEGR in power MOSFETs, particularly under high drain bias. Modern trench-based Si-power devices remain susceptible to these effects and can additionally exhibit localized microdose damage that accelerates parametric degradation [51]. Non-destructive SEUs and SETs in power control and feedback circuitry can induce transient regulation errors, missing switching pulses, or sustained oscillations in switching converters, compromising output stability and availability [50].

Wide-Bandgap (WBG) semiconductors, notably Gallium Nitride (GaN) High-Electron-Mobility Transistors (HEMT) and Silicon Carbide (SiC) MOSFETs, have emerged as attractive alternatives due to their high breakdown fields and efficiency. The radiation response of these devices remains strongly technology- and bias-dependent. GaN devices exhibit threshold voltage shifts and transconductance degradation driven by defect formation and carrier removal mechanisms [52]. At the device level, however, GaN power transistors have demonstrated susceptibility to SEB with significant device-to-device variability, necessitating conservative voltage derating in space applications [53]. SiC power MOSFETs generally show improved tolerance to cumulative damage but remain vulnerable to heavy-ion-induced SEB, requiring careful biasing and protection strategies to bound failure risk [54].

B. PHOTONICS

Photonics form the optical signal path of OCTs, integrating passive and active functions with electronic control on a single platform to enable high-speed signal generation, modulation, routing, and detection. A recent comprehensive review of radiation effects in PICs for optical satellite communication links provides a broad and systematic overview of the state-of-the-art [11]. This section builds upon that review and synthesizes its findings with additional studies to highlight radiation responses and design considerations for photonics in space.

1) OPTICAL ROUTING

Optical routing in OCT photonic subsystems uses integrated optical waveguides, resonant structures, and optical fibers to transport, split, and spectrally filter optical signals between functional blocks. In PICs, waveguides form the fundamental routing elements and enable interferometric devices such as Ring Resonators (RRs) and Mach-Zehnder Interferometers (MZIs), which rely on controlled optical phase accumulation for wavelength selective operation. Radiation affects these structures primarily through changes in material optical properties, leading to refractive index variation and, in some cases, additional propagation loss. Both TID and DD contribute to these effects, with their relative impact strongly dependent on material platform, waveguide geometry, cladding configuration and dose rate [11].

Since resonant photonic devices rely on precise optical phase accumulation, radiation-induced modifications of material optical constants directly translate into shifts of resonance wavelength and interference conditions. These changes originate from trapped charge formation, defect generation, surface oxidation, mid-gap state absorption, and volume compaction or expansion [24]. Resonant structures such as RRs and MZIs are therefore frequently used as sensitive probes of refractive index variations in integrated waveguides. Resonance wavelength shifts have been experimentally observed in fiber-based resonant and interferometric

structures, demonstrating sensitivity to cumulative, material dependent parametric changes [55]. Deliberate material selection and mode confinement can improve radiation tolerance. In particular, SiC/Silicon Dioxide (SiO_2) waveguide platforms exploit opposite-sign refractive index changes in core and cladding to minimize net effective index drift under ionizing radiation [56]. Similarly, Si-photonic waveguides with increased thickness and strong mode confinement exhibit reduced sensitivity to refractive index variations and propagation loss, even at high accumulated dose, making geometry optimization an effective hardening strategy [57]. Experimental studies on Si RRs confirm this tolerance, with passivated devices showing no systematic degradation in Q Factor (Q), free spectral range, or peak position up to 100 Mrad of gamma irradiation [58], and resonance wavelength shifts limited to 0.4 pm/krad at 300 krad [59]. Indium Gallium Arsenide Phosphide (InGaAsP)/Indium Phosphide (InP) RRs similarly exhibit limited degradation at 320 krad, with Q variations of approximately 13%, Extinction Ratio (ER) variations up to 4%, and linear resonance red-shifts [60].

Charged particle strikes can generate OSETs through rapid creation of dense electron–hole clouds, leading to transient free-carrier absorption and phase shifts. Recovery is governed by carrier diffusion and recombination processes, with characteristic timescales ranging from pico- to nanoseconds depending on material properties, waveguide geometry, and strike conditions [28], [61]. Pulsed laser experiments on integrated Si-waveguides have demonstrated OSETs with transient transmission reductions on the order of several percent, with substantially larger excursions observed only under extreme carrier injection conditions used to emulate worst-case events [29]. Mitigation strategies for radiation effects in optical fibers primarily rely on material and structural engineering, including optimized core and cladding compositions, radiation-hardened and microstructured fiber designs, and appropriate wavelength selection. System-level approaches such as link margin allocation and multi-fiber redundancy can further improve robustness, whereas shielding and protective coatings provide limited benefit for highly penetrating radiation [62].

2) MODULATION AND AMPLIFICATION

Optical modulation in OCT photonic subsystems is commonly implemented using integrated Mach-Zehnder Modulators (MZMs) or Ring Modulators (RMs), relying on electro-optic mechanisms such as plasma dispersion, carrier-density modulation, the quantum-confined Stark effect, or the Pockels effect, depending on the material platform. Si, InP, and Lithium Niobate ($LiNbO_3$) are the dominant technologies for high-speed integrated modulators. Radiation testing across these platforms shows that modulators typically exhibit parametric degradation, with devices generally remaining operational over radiation levels comparable to or exceeding typical mission requirements. In Si-photonic MZMs, ionizing radiation primarily affects doped p-n junction phase shifters through defect generation and charge trapping, leading to reduced modulation efficiency, extinction ratio degradation, and effective refractive index shifts [63]. Recent device generations demonstrate significantly improved tolerance through optimized doping profiles and reduced low-doped regions [64], [65]. DD effects in modulators depend strongly on particle type and device material. Si-based modulators demonstrate high resilience to neutron irradiation [64], whereas InP-based MZMs show pronounced sensitivity to high proton fluence, with near-complete suppression of modulation response observed [66]. $LiNbO_3$ modulators exhibit a distinct degradation pathway, where irradiation primarily increases insertion loss at high fluence [67]. This behavior reflects the intrinsic radiation robustness of the Pockels effect compared to carrier-based modulation mechanisms. OSET studies on Si-MZMs show strong dependence on modulator bias point, with maximum sensitivity at quadrature operation [68]. These transients are short-lived and can be mitigated at the system level through coding, interleaving, or link margin.

Optical amplification in OCTs is commonly implemented using semiconductor optical amplifiers or Erbium-Doped Fiber Amplifiers (EDFAs), particularly in architectures employing external modulation. Radiation effects in optical amplifiers are dominated by cumulative degradation, with performance impact primarily arising from attenuation in the gain medium. Irradiation studies on EDFAs exposed to electron and proton radiation report pronounced output power degradation and noise figure increase with increasing dose [69]. EDFA usability is therefore primarily constrained by cumulative damage, with acceptable performance generally limited to low-dose orbital environments. The dominant degradation mechanism in doped optical amplifiers is accumulation of radiation-induced loss in the doped fiber due to defect and color-center formation [70]. More studies show that amplifier radiation tolerance depends strongly on fiber composition and pump operating conditions, with radiation-hardened designs exhibiting substantially reduced gain degradation. Irradiation experiments further indicate weak temperature dependence of gain degradation kinetics and support extrapolation to low dose-rate space environments, where performance remains dominated by radiation-induced attenuation in the doped fiber [71].

3) LIGHT SOURCES

Light sources in OCT photonic subsystems use direct band gap semiconductor materials to enable efficient optical gain and emission at infrared wavelengths. The most commonly employed material platforms include InP, GaAs, Gallium Antimonide (GaSb), and their alloys, supporting device architectures such as Fabry–Pérot (FP), Distributed Feedback (DFB), and Distributed Bragg Reflector (DBR) lasers. Radiation effect studies on laser sources typically evaluate variations in threshold current, output optical

power, slope efficiency, emission wavelength, and noise characteristics [11].

The radiation response of semiconductor lasers is largely governed by DD, which degrades minority carrier lifetime through defect generation in the active region and surrounding layers. This mechanism manifests primarily as increased threshold current and reduced output power, while ionizing radiation generally produces negligible direct damage to the gain medium. Laser designs employing heterostructures, quantum wells, strained layers, and optimized carrier confinement exhibit substantially improved radiation tolerance, with partial recovery often observed under forward bias due to injection-enhanced annealing effects [72].

Experimental qualification of InP-based multi-quantum-well lasers under radiation demonstrates that DD from hadrons is the dominant degradation mechanism, whereas TID up to 100 kGy induces minimal performance change [73]. Threshold current increases of only a few milliamperes are typically observed at end-of-life fluence levels, while lasing operation and spectral integrity are preserved. Investigations on DBR cavity lasers fabricated using generic PIC integration platforms indicate high robustness to both gamma and proton irradiation at dose and fluence levels relevant to LEO missions. In these devices, no systematic degradation of output power or threshold current is observed, while small, monotonic wavelength shifts (sub-nanometer) can occur under ionizing radiation [74], [75]. These shifts are attributed to radiation-induced refractive index changes in passive grating sections rather than degradation of the gain region.

Advanced light source architectures based on Quantum Dot (QD) active regions further enhance radiation tolerance through strong carrier confinement and reduced active volume. Proton irradiation studies demonstrate that QD lasers maintain stable threshold behavior, low relative intensity noise, and strong resilience to optical feedback over fluence levels exceeding those encountered in space missions analyzed in this work [76].

4) OPTICAL DETECTION

Optical detection forms the receiver interface of OCTs by converting incident optical signals into electrical signals for amplification and processing. Avalanche Photodiodes (APDs) are widely used in high bit-rate, long-haul optical communication links due to their internal gain and improved sensitivity, although p-i-n Photo Detectors (PDs) remain attractive for their lower noise, simpler biasing, higher maximum optical power, and improved radiation robustness. Key radiation-sensitive performance parameters include responsivity, dark current, gain (for APDs), and bandwidth. Common detector material systems include SiGe for near-infrared wavelengths and Indium Gallium Arsenide (InGaAs)/InP or Indium Arsenide (InAs)-based heterostructures.

DD introduces defects in the absorption and multiplication regions, leading to increased dark current, degraded carrier lifetime, and higher noise levels. Proton irradiation studies on InGaAs/InP single-photon APDs show that detector parameters remain largely stable at fluences below 10^9 cm^{-2}, while higher fluences induce strong increases in dark current and shifts in breakdown voltage, defining a DD-limited operational envelope [77]. Similar trends are observed in InAs APDs, where high proton fluence leads to measurable degradation in avalanche gain and leakage current, while responsivity remains largely unaffected across a wide range of irradiation energies and fluences [78]. Neutron irradiation of waveguide-integrated SiGe p-i-n PDs shows susceptibility to carrier removal effects, yet devices remain fully operational with no meaningful degradation in responsivity, bandwidth, or capacitance, indicating substantial DD tolerance of integrated receiver structures [79]. Partial recovery of radiation-induced noise through annealing has also been demonstrated, indicating the presence of metastable defect populations [77].

TID effects in PDs depend strongly on device geometry and integration approach. TID testing of SiGe p-i-n PDs under X-ray irradiation shows no measurable degradation in dark current, frequency response, or electro-optical conversion efficiency, even when accounting for back-end-of-line dose enhancement from nearby high-Z materials [80]. These results indicate that integrated PDs can exhibit strong intrinsic tolerance to ionizing radiation.

SEEs in PDs manifest as transient current disturbances caused by localized charge generation along the particle track. Pulsed-laser and heavy-ion studies on SiGe p-i-n PDs show that OSETs amplitude and duration depend on device geometry, biasing, and optical operating point, with illuminated detectors exhibiting reduced transient peaks due to field screening by photo-generated carriers [61]. Statistical analysis demonstrates that these transients can induce bit errors in realistic modulation schemes, but system-level and device-level hardening techniques can effectively mitigate their impact without permanent performance degradation [81].

5) SUMMARY OF PHOTONIC RADIATION TOLERANCE

To provide a systematic comparison of experimentally measured radiation tolerance across photonic technologies relevant to OCTs, Table 1 consolidates representative results from literature.

IV. RADIATION ENVIRONMENT

This section analyzes the radiation conditions across different orbital regimes, focusing on trapped particles, Solar Energetic Particles (SEPs), and Galactic Cosmic Rays (GCRs). The analysis is conducted using SPENVIS [82], and follows a methodology similar to [83]. This section provides radiation flux and fluence spectra for various energy and LET values, serving as a foundation for further SEE estimation and

TABLE 1. Summary of representative experimentally measured radiation tolerance levels for photonic PIC devices relevant to OCT architectures. Radiation types are listed per study. Dose is reported as TID where applicable, and fluence in cm^{-2} for particle irradiation.

Device	Radiation	Dose or Fluence	Key Observed Effect	Reference
Si waveguide (3 μm)	Gamma	41 Mrad	Stable performance	[57]
Si waveguide (3 μm)	Proton	1×10^{16} cm^{-2}	Stable performance	[57]
Si waveguide	Gamma	100 Mrad	No significant dose dependent changes	[58]
SiC waveguide	Gamma	10 Mrad	Negligible insertion losses	[56]
Si/SiO_2 waveguide	Gamma	300 krad	Spectral shift up to 0.03 pm/krad	[59]
Si on insulator RR	Gamma	300 krad	Spectral shift up to 0.4 pm/krad	[59]
Si RR	Gamma	100 Mrad	No significant dose dependent changes	[58]
InGaAsP/InP RR	Gamma	320 krad	ΔQ 13%, ΔER 4%, red-shift 810 pm	[60]
Si MZM	X-ray	130 Mrad	Phase-shift of 10% at 60 Mrad and 1 V bias	[63]
Si MZM	Neutron	1.2×10^{15} cm^{-2}	No significant degradation	[63]
Si MZM	Neutron	3×10^{16} cm^{-2}	No phase shift degradation	[64]
Si MZM	X-ray	1 Grad	Highest doping concentration showed performance degradation	[65]
InP MZM	Proton	1×10^{15} cm^{-2}	Near-complete modulation suppression	[66]
$LiNbO_3$ MZM	Ion	1×10^{16} cm^{-2}	Degradation of operational parameters and significant insertion loss	[67]
EDFA	Electron	1 Mrad	Output power degradation, noise figure increase	[69]
InGaAsP/InP laser	Proton	2×10^{14} cm^{-2}	DD-driven threshold current increase	[73]
InGaAsP/InP laser	Gamma	10 Mrad	No measurable damage	[73]
InP DBR laser	Gamma	50 krad	Wavelength shift of emitted peak in linear correlation to TID	[74]
InP DBR laser	Gamma	106 krad	No radiation induced degradation	[75]
InP DBR laser	Proton	1.5×10^{11} cm^{-2}	No radiation induced degradation	[75]
InAs/GaAs QD laser	Proton	7×10^{13} cm^{-2}	Stable behaviour, 1 dB Hz^{-1} increase of relative intensity noise	[76]
InGaAs/InP APD	Proton	10^{8}–10^{13} cm^{-2}	Dark current increase, breakdown voltage shift, and dark count increase	[77]
InAs APD	Proton	10^{9}–10^{11} cm^{-2}	Gain and leakage degradation at high fluence	[78]
SiGe p-i-n PD	Neutron	7.5×10^{12} cm^{-2}	Susceptible to carrier removal (DD effect), but no meaningful impact to performance	[79]
SiGe p-i-n PD	X-ray	5 Mrad	No significant changes in performance	[80]

assessment. Dose rate effects and time-dependent annealing processes are not explicitly modeled in this analysis, but may significantly affect component response.

A. ORBITAL REGIMES

The anticipated deployment spans multiple orbital regimes, namely SSO, LEO, and MEO, selected to capture the representative range of radiation environments relevant to emerging OCT architectures. The orbital parameters summarized in Table 2 represent conservative, near worst-case configurations within each regime, with altitudes ranging from 567 km for SSO to 8200 km for MEO, and inclinations between 87° and 97.7°. A uniform 6 year operational lifetime is assumed across all regimes to enable consistent comparison of radiation exposure. Results are normalized to annual values based on this duration. The LEO configuration reflects a worst-case low-altitude environment with elevated trapped particle fluxes, whereas the MEO case is intentionally positioned comfortably in the transition region between the inner and outer radiation belts, consistent with recently authorized commercial orbital deployments [84]. Unless stated otherwise, radiation flux and fluence spectra are computed assuming 1 g cm^{-2} Aluminium (Al) shielding (equivalent to 3.7 mm), a standard baseline for preliminary radiation assessments.

B. TRAPPED PARTICLES

Earth's magnetosphere traps energetic particles, forming the Van Allen radiation belts [85]. These belts consist of an inner region, dominated by high-energy protons and electrons, and an outer region, primarily composed of electrons [86]. A third transient belt has also been observed, where ultra-relativistic electrons remain trapped for extended periods due to wave-particle interactions [87]. The belts are highly dynamic, undergoing rapid flux variations from geomagnetic storms and longer-term changes linked to the solar cycle [88]. A key feature of the inner belt is the South Atlantic Anomaly (SAA), where Earth's magnetic field allows trapped particles to reach lower altitudes, increasing radiation exposure for spacecraft [89]. The SAA is gradually drifting westward due to slow geomagnetic field variations [88].

TABLE 2. Overview of mission orbits for OCTs across different orbital regimes, including altitude and inclination parameters.

Orbit	Altitude / km	Inclination / °
SSO	567	97.7
LEO	1200	87.0
MEO	8200	87.0

This study employs NASA's AP8-min and AE8-max models via SPENVIS, which have been the historical standard for radiation belt environments. AP8-min was selected for protons, as the highest trapped proton intensity occurs during solar minimum. AE8-max was selected for electrons, as the highest trapped electron intensity occurs during solar maximum. However, these models are static and do not account for solar modulation of trapped fluxes [90]. The newer AP9/AE9 models improve upon this by incorporating multi-cycle data and a probabilistic approach to environment definition. Nevertheless, comparisons with in situ data show

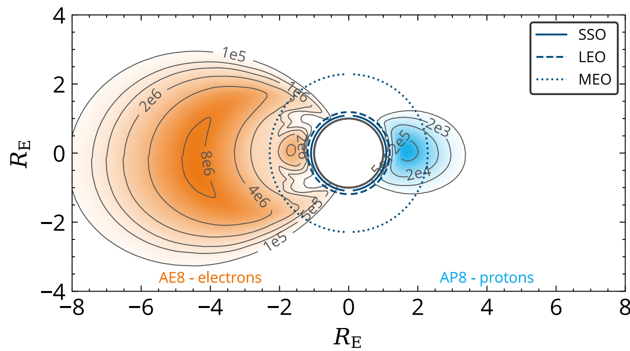

FIGURE 3. Earth's radiation belts visualization with the three orbits using AE8 and AP8 models, showing integral flux contours in $\mathrm{cm^{-2}\,s^{-1}}$ for electrons (>0.6 MeV) on the left and protons (>10 MeV) on the right.

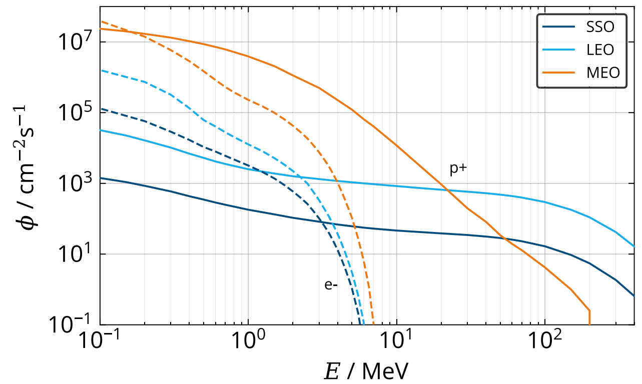

FIGURE 4. Integral trapped particle fluxes for SSO, LEO, and MEO orbits. Solid lines represent protons (p+) (AP8-min), while dashed lines represent electrons (e-) (AE8-max). Shielding Line color indicates the orbital regime.

that while AP9 better captures the spatial distribution of the SAA, flux predictions differ regionally from AP8/AE8, with higher predictions in low-inclination LEO and the slot region but lower predictions elsewhere, requiring mission-specific validation [91]. For the high-inclination orbits considered in this work, these differences are not expected to affect the relative ranking of orbital regimes or the identification of dominant radiation sources. The qualitative conclusions regarding which environment is most severe and which radiation source dominates in each regime are therefore expected to be robust against model choice, though absolute dose and fluence values should be validated with AP9/AE9 or in-flight data for detailed mission-specific qualification.

Figure 3, generated using the radbelt Python package with the international geomagnetic reference field [92], [93], [94], illustrates the spatial distribution of trapped particles. The inner belt, centered at 1.5 Earth radii (R_E), contains both protons and electrons, while the outer belt, around 4 R_E, consists primarily of electrons. Between them, the slot region exhibits reduced flux due to wave-particle losses. Empirical models provide static representations, however observations reveal rapid variations occurring within minutes during solar events, as well as gradual long-term shifts [88].

Figure 4 presents the integral trapped proton and electron fluxes for the SSO, LEO, and MEO orbital regimes. Solid lines denote protons, while dashed lines denote electrons, with colors indicating the orbit class. At low energies, the trapped proton flux in MEO is significantly higher than in LEO and SSO. However, above approximately 20 MeV, the MEO proton flux drops sharply, and LEO and even SSO exhibit higher flux levels. In contrast, trapped electron fluxes show a similar spectral shape across all orbits, with MEO consistently presenting the highest levels over the full energy range. These trends indicate that SEEs driven by high-energy protons are the dominant radiation concern in lower orbits, whereas TID effects from low-energy protons and electrons are more critical in MEO.

C. SOLAR PARTICLES

SEPs are high-energy protons, electrons, and ions originating from solar activity. Their flux and energy follow the 11 year solar cycle, with peak emissions occurring during Solar Particle Events (SPEs) and Coronal Mass Ejections (CMEs). While these events are more frequent at solar maximum, they can occur unpredictably throughout the cycle [89]. SEPs contribute significantly to the space radiation environment, particularly in high-altitude and interplanetary missions.

The analysis employs CREME-96 for peak 5 minute flux estimations and ESP-PSYCHIC for long-term fluence predictions at a 95% confidence level. However, these models have inherent limitations, particularly in accurately representing the full energy spectrum of SEPs [95]. While current models focus primarily on the MeV range, lower-energy particles can also contribute to material degradation and charge accumulation effects [96].

As shown in Figure 5, solar particle environments exhibit broadly similar spectral shapes across SSO, LEO, and MEO, with differences primarily driven by geomagnetic shielding. Solid lines represent protons, while dashed lines represent helium-4 ions, with line color indicating the orbital regime. An overview of representative proton flux and fluence levels is provided in Table 3. For both solar flare fluxes and cumulative fluence, SSO and LEO benefit from stronger geomagnetic protection, resulting in reduced exposure compared to MEO. In contrast, MEO consistently experiences the highest proton and ion levels due to diminished magnetic shielding. These results indicate that SEPs constitute a significant radiation concern for high altitude and deep space missions.

D. GALACTIC COSMIC RAYS

GCRs are very high-energy particles originating from outside the solar system, arriving isotropically from all directions. Their composition consists of approximately 85% protons, 13% alpha particles, 2% electrons, and a smaller fraction

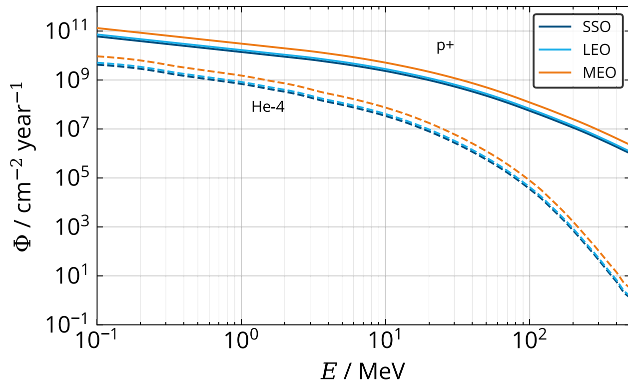

FIGURE 5. Annualized integral solar particle fluence spectra computed using the ESP-PSYCHIC model. Protons (p+) (solid) and helium-4 ions (dashed) fluence levels are shown for SSO, LEO, and MEO orbits assuming 1 g cm^{-2} Al shielding. Values are normalized to one year to allow scaling to arbitrary mission durations.

TABLE 3. Overview of integral solar flare instantaneous proton fluxes determined using the CREME-96 model and total proton fluences (trapped and solar) determined using the ESP-PSYCHIC model, across different orbital regimes and representative energy levels, assuming 1 g cm^{-2} Al shielding. Fluence values are normalized per year to allow scaling to arbitrary mission durations.

Orbit	E / MeV	ϕ / cm^{-2} s^{-1}	Φ / cm^{-2} yr^{-1}
SSO	70	2.54×10^6	8.42×10^8
	120	6.97×10^5	5.60×10^8
	200	1.87×10^5	1.73×10^8
LEO	70	3.05×10^6	1.27×10^9
	120	8.37×10^5	9.38×10^9
	200	2.23×10^5	3.47×10^9
MEO	70	5.58×10^6	6.38×10^8
	120	1.54×10^6	2.13×10^8
	200	4.12×10^5	3.28×10^7

of heavier nuclei, with abundances differing from universal elemental distributions [97], [98]. GCR fluxes exhibit an inverse correlation with solar activity, with higher fluxes occurring during solar minimum due to the weakened heliospheric magnetic field [99], [100]. While supernova remnants have traditionally been considered the primary source, recent evidence suggests that superbubbles may contribute significantly, particularly in the transition between GCR and extra-GCR, which occurs around 10^{17} eV for protons [101].

This analysis uses the ISO 15390 model under solar minimum conditions to represent worst-case GCR exposure, as implemented in SPENVIS. However, model accuracy varies with particle type, energy range, and epoch, presenting challenges in representing the complex mixture of particles and the influence of geomagnetic shielding [102]. Figure 6 shows the shielded proton and ion fluence for the three orbital regimes. Across all orbits, the proton fluence varies depending on the position of the orbit with respect to the radiation belt. MEO has slightly more high energy protons, while LEO has more lower energy protons. SSO has generally less proton fluence. The ions show a slight increase in fluence from SSO to LEO to MEO. Key LET spectra values are summarized in Table 4.

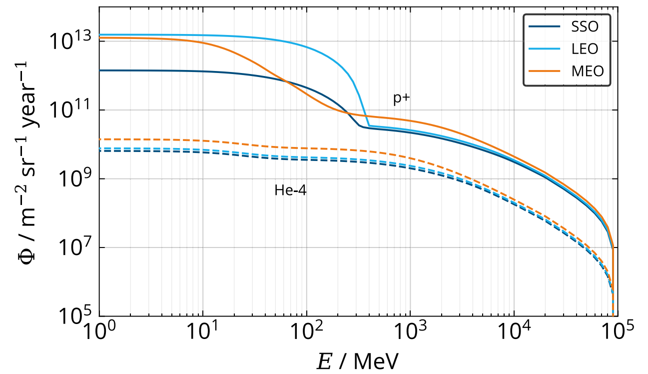

FIGURE 6. Annualized shielded fluence comparison of GCRs and solar protons (p+) and helium-4 ions across orbital regimes, assuming 1 g cm^{-2} Al shielding. Values are normalized to one year to allow scaling to arbitrary mission durations.

TABLE 4. Annualized shielded particle fluxes and fluences evaluated at representative LET thresholds relevant for SEEs. LET values of 15, 38, and 60 MeV cm^2 g(Si)$^{-1}$ correspond to typical SEE sensitivity levels. Assuming 1 g cm^{-2} Al shielding.

Orbit	LET / MeV cm^2 g(Si)$^{-1}$	ϕ / cm^{-2} s^{-1}	Φ / cm^{-2} yr^{-1}
SSO	15	1.11×10^7	3.95×10^{11}
	38	2.57×10^6	8.08×10^{10}
	60	9.85×10^5	3.10×10^{10}
LEO	15	1.35×10^7	2.62×10^{12}
	38	3.10×10^6	4.67×10^{11}
	60	1.19×10^6	1.72×10^{11}
MEO	15	2.48×10^7	1.01×10^{12}
	38	5.74×10^6	3.23×10^{12}
	60	2.20×10^6	1.27×10^{11}

E. DOSE ANALYSIS

The radiation dose analysis quantifies the cumulative effects of particle interactions in photonic-electronic systems across different orbital regimes. TID and TNID effects are analyzed as a function of Al shielding thickness to evaluate mitigation strategies for different mission profiles.

1) TOTAL IONIZING DOSE

TID calculations are performed using SHIELDOSE-2, which models radiation transport through a centered Al sphere, as implemented in SPENVIS. While this method provides a reliable approximation, its simplified detector assumptions may not fully represent modern semiconductor structures, where CMOS scaling effects and device geometry significantly influence radiation response [103], [104]. More advanced modeling approaches, such as compact physics-based models, incorporate oxide-trapped charge, interface traps, and their impact on device behavior, improving

predictive accuracy for MOS technologies [105]. However, these methods require detailed device parameters, making them less practical for early-stage or conceptual mission analysis.

Table 5 shows the accumulated annual dose versus shielding thickness across different orbits. Shielding is particularly effective in MEO, where TID levels decrease sharply with increasing Al thickness. At approximately 7.5 mm of shielding, MEO dose levels drop below those of lower orbits, though this result should be interpreted considering model limitations. For a reference shielding thickness of 5 mm, LEO experiences TID levels roughly 7.5 times higher than SSO, while MEO exposure is approximately 4.5 times that of LEO.

TABLE 5. Comparison of annualized TID and TNID for representative Al shielding thicknesses in SSO, LEO, and MEO. Thickness range selected to reflect typical avionics enclosure and board-level shielding achievable in SmallSat-class satellites.

Orbit	Al / mm	TID / krad(Si) yr^{-1}	TNID / MeV $g(Si)^{-1}$ yr^{-1}
SSO	2	2.77	1.22×10^7
	3	1.32	8.98×10^6
	4	0.73	7.32×10^6
	5	0.46	6.30×10^6
	6	0.33	5.70×10^6
	7	0.26	5.20×10^6
	8	0.23	4.75×10^6
LEO	2	12.79	9.35×10^7
	3	6.88	7.83×10^7
	4	4.50	7.07×10^7
	5	3.35	6.43×10^7
	6	2.80	6.15×10^7
	7	2.50	5.85×10^7
	8	2.33	5.57×10^7
MEO	2	189.72	4.30×10^8
	3	76.97	1.58×10^8
	4	33.69	7.65×10^7
	5	15.17	4.00×10^7
	6	7.25	2.98×10^7
	7	3.82	2.22×10^7
	8	2.32	1.66×10^7

2) TOTAL NON-IONIZING DOSE

The JPL (Si) 1996 damage curve, implemented in SPENVIS, is used to estimate TNID across different orbital regimes, with results shown in Table 5. While widely used, this model has known limitations, particularly in handling low-energy electron damage and NIEL dependencies. More advanced models, such as the athermal-recombination-corrected model and NIEL approaches with additional corrections, show better agreement with experimental data, improving predictions across different energy ranges [106], [107].

The results indicate that LEO experiences approximately ten times higher TNID levels than SSO due to inner Van Allen belt interactions. However, beyond approximately 4.5 mm of shielding, MEO TNID drops below LEO levels. This crossover is explained by the trapped proton energy spectrum as shown in Figure 4. The MEO trapped proton flux falls sharply above approximately 20 MeV, whereas LEO maintains higher flux at these energies. At increased shielding thickness, lower-energy particles are effectively attenuated, and the residual TNID is dominated by high-energy protons, for which LEO presents the more severe environment.

TABLE 6. Relative radiation source contributions across orbital regimes, corresponding to the absolute values in Table 7. No information indicates a contribution below 0.1%.

Orbit	Source	HEH	Low-LET	High-LET	TID	TNID
SSO	Trapped	54.1%			74%	53.7%
	Solar	44%	79.3%	7.1%	26%	46.3%
	GCR	1.9%	20.7%	92.9%		
LEO	Trapped	94.4%			94.9%	94.2%
	Solar	5.4%	79.6%	7.1%	5.1%	5.8%
	GCR	0.2%	20.4%	92.9%		
MEO	Trapped	92.8%			98.8%	90.3%
	Solar	6.9%	79.6%	7.4%	1.2%	9.7%
	GCR	0.3%	20.4%	92.6%		

F. RELATIVE CONTRIBUTIONS

To identify the dominant radiation source for each orbital regime, Table 6 and Table 7 summarise the annualized radiation levels and relative contributions of trapped particles, solar particles, and GCRs to key radiation metrics. High Energy Hadrons (HEHs), defined here as protons above 20 MeV, are relevant for both proton-induced SEEs through nuclear reactions and cumulative dose contributions. Trapped protons dominate the HEH fluence across all orbits, contributing over 90% in LEO and MEO, although in SSO the trapped and solar contributions are more comparable at 54% and 44% respectively. For low-LET ions, represented by helium ions above 15 MeV/n, solar particles are the dominant source across all regimes at approximately 80%. In contrast, the high-LET environment, represented by iron ions above 60 MeV/n, is overwhelmingly dominated by GCRs at over 92% across all orbits. This source crossover from solar-dominated at low energies to GCR-dominated at high energies is consistent across all orbital regimes. Trapped particles also dominate TID and TNID in all orbits, with their contribution increasing from SSO to MEO.

V. DISCUSSION

The preceding sections have examined radiation effect mechanisms, OCT technologies, and operational environments. By combining standard radiation environment models with a structured multi-technology vulnerability assessment, direct identification of where radiation effects are transferable across orbital regimes and where orbit-specific adaptation is necessary becomes possible. This section synthesizes these results to identify dominant failure mechanisms, system-level implications, and practical considerations for radiation assurance. Table 7 summarizes the annualized radiation levels across orbital regimes, while Table 8 and Table 9 consolidate component-level failure mechanisms, providing a basis for orbit-specific design strategies.

TABLE 7. Annualized total radiation levels across orbital regimes assuming 4 mm Al shielding, showing HEH fluence (integral proton fluence above 20 MeV from trapped, solar, and GCR sources), low-LET ion fluence (helium ions above 15 MeV/n from solar and GCR sources), high-LET ion fluence (iron ions above 60 MeV/n from solar and GCR sources), TID, and TNID. All values are normalized per year to allow scaling to arbitrary mission durations. The corresponding relative source contributions are provided in Table 6.

Orbit	HEH / cm^{-2} yr^{-1}	Low-LET / cm^{-2} yr^{-1}	High-LET / cm^{-2} yr^{-1}	TID / krad(Si) yr^{-1}	TNID / MeV $g(Si)^{-1}$ yr^{-1}
SSO	2.25×10^{9}	2.26×10^{7}	1.50×10^{4}	0.73	7.32×10^{6}
LEO	2.21×10^{10}	2.71×10^{7}	1.77×10^{4}	4.50	7.07×10^{7}
MEO	3.17×10^{10}	4.96×10^{7}	3.18×10^{4}	33.69	7.65×10^{7}

A. ORBITAL DEPENDENCE

The radiation response of OCTs is strongly orbit dependent, with each mission class imposing a distinct balance between cumulative dose and SEE exposure as shown in Table 7. These differences directly shape system level design constraints and qualification strategies. In SSO, the radiation environment is comparatively mild. SEEs inducing particles have a low flux, and TID accumulation is typically bounded to low tens of krad(Si) over multi-year mission lifetimes. As a result, both electronic and photonic subsystems retain wide operational margins, enabling the use of COTS or lightly qualified components provided that basic SEE mitigation is applied. LEO missions are dominated by trapped protons, making proton-induced SEEs the primary system-level risk. While TID levels remain moderate, frequent SEE interactions impose availability constraints on digital electronics and mixed-signal subsystems. Photonic components are exposed to the same environment but are primarily affected through gradual margin erosion rather than immediate loss of functionality. In MEO, the radiation environment becomes fundamentally harsher. It should be noted that standard environment models and tools such as SPENVIS provide mission-average estimates and may underestimate short-term flux enhancements due to geomagnetic storms, SPEs, and outer-belt injections, particularly for high-altitude LEO and MEO. Additionally, any transfers from lower orbit to higher orbits are not included in the analysis. Elevated TID combined with increased heavy-ion flux shifts the design driver from transient disturbance tolerance to long-term survivability. Performance margins must be explicitly budgeted at mission planning, as cumulative degradation defines end-of-life capability and the probability of destructive SEEs is higher.

B. FAILURE MODES

Radiation-induced failure modes differ fundamentally between electronics and photonics, driven by distinct physical mechanisms and temporal characteristics.

1) ELECTRONICS

Failure modes in electronic components originate from ionizing and DD processes described in Section II, with architecture-dependent manifestations detailed in Section III and consolidated in Table 8. The key distinction is between cumulative parametric degradation and stochastic transient events that directly threaten functional availability. Ionizing radiation drives gradual degradation through threshold voltage shifts, leakage current increase, and noise degradation, while rapid charge collection at sensitive junctions produces SEEs when the deposited charge exceeds the device-specific critical charge. The manifestation is architecture dependent: SRAM-based configuration memory exhibits high SEU sensitivity, flash memories fail predominantly through peripheral circuitry degradation, mixed-signal circuits experience parametric drift and noise increase, and power devices are susceptible to destructive SEB and SEGR. Device scaling introduces competing effects, with thinner gate oxides improving TID tolerance and reduced node capacitance increasing susceptibility to transient charge collection.

2) PHOTONICS

In contrast, photonic components predominantly exhibit cumulative parametric degradation, with technology-specific responses detailed in Section III and consolidated in Table 9. Lattice displacement and ionizing radiation induce defect formation that degrades carrier lifetimes, alters the refractive index, and increases optical absorption, with severity strongly dependent on the material system. OSETs occur through free-carrier generation but recover on pico- to nanosecond timescales through carrier recombination and diffusion. Although OSETs can induce transient bit errors under realistic modulation schemes, their short recovery timescales and their amenability to system-level mitigation through coding, interleaving, and link margin allocation distinguish them from the discrete, availability-threatening failure modes characteristic of electronic subsystems. Degradation manifests predominantly as monotonic shifts in most passive and active devices, although modulator and amplifier technologies may exhibit threshold degradation at high fluence.

C. SYSTEM ARCHITECTURE

The asymmetry in failure modes between electronics and photonics directly shapes viable system architectures and mitigation strategies across orbital regimes. Such systems leverage component technologies with well characterized radiation response across a broad range of orbital environments, enabling design commonality and reduced non-recurring engineering costs, though mission-specific margin allocation and qualification remain necessary. SRAM-based FPGAs emerge as viable candidates when

TABLE 8. Overview of dominant radiation-induced failure mechanisms for electronic components in OCT avionics across orbital regimes. Mechanisms are listed for each orbit class assuming 4 mm Al shielding. Failure severity and manifestation exhibit significant device-to-device variability within each technology class, particularly for COTS components where process variations and architecture differences can alter radiation response by orders of magnitude. Dose-rate effects are also not accounted for.

Technology	SSO	LEO	MEO	References
FPGA	SEE: SRAM configuration memory corruption, logic upsets, SEFIs.	TID: I/O degradation, propagation delay increase. SEE: SRAM configuration memory and BRAM corruption, logic upsets, SEFIs, SELs under high I/O bank bias.	TID: I/O degradation, timing delays. SEE: Configuration corruption (including MBUs), logic upsets, SEFIs, SELs.	[22], [31]–[36]
MCU	SEE: Register and memory corruption, control-flow errors, functional interrupts.	TID: Parametric drift, current leakage. SEE: Register and memory corruption, SEFIs, resets and hangs, flash errors.	TID: Flash memory and peripheral degradation, current leakage. SEE: State corruption, loss of writability in flash memory, SEFIs, destructive events.	[22], [37], [38]
Mixed-signal	SEE: Control-logic upsets, transient misconfiguration, bias network perturbations.	TID: Threshold voltage shifts, leakage current increase, transconductance reduction, excess low-frequency noise, gain, offset, linearity, SNR, and I/O degradation. DD: Additional threshold shifts. SEE: Control-logic upsets, SEFIs, transient misconfiguration, bias network perturbations.	TID: Threshold voltage shifts, leakage current increase, transconductance reduction, excess low-frequency noise, gain, offset, linearity, SNR, I/O degradation, functionality loss. DD: Additional threshold shifts, gradual gain reduction and noise increase in GaAs-based circuits. SEE: All types of non-destructive events, potential destructive events in embedded digital logic, reduced SELs susceptibility in SiGe technologies.	[5], [39]–[44]
Memory	SEE: Data corruption in volatile memories (SEUs), transient memory state disturbances.	TID: Peripheral circuitry degradation, increased leakage currents. SEE: Volatile and NVM data and state corruption (SEUs, SEFIs), flash write and erase margin loss dominated by peripheral and charge-pump degradation.	TID: Retention loss, peripheral and charge-pump failure in NVMs, loss of writability in NVMs. DD: Material degradation in emerging NVMs affecting long-term reliability. SEE: Volatile and NVM data corruption (including MBUs), memory state machine interrupts, destructive events.	[45]–[49]
Power	SEE: Non-destructive events in control and feedback logic causing transient regulation errors, missing switching pulses, and oscillations. Destructive events in Si-power devices under high bias.	TID: Current leakage, threshold voltage shifts, increased on-resistance, reduced breakdown margin, bipolar gain degradation. DD: Additional threshold shifts, opto-coupler current transfer ratio loss. SEE: Non-destructive events in control and feedback logic causing transient regulation errors, missing switching pulses, and oscillations. Destructive events in Si-power devices.	TID: Current leakage, threshold voltage shifts, increased on-resistance, breakdown margin loss, bipolar gain degradation, degraded PWM accuracy and switching stability. DD: Additional threshold shifts, opto-coupler current transfer ratio loss, transconductance loss. SEE: Non-destructive events in control and feedback paths. Destructive events in Si- and WBG-power devices.	[50]–[54]

paired with configuration scrubbing, though flash-based alternatives may be preferred for MEO missions in lower TID classes. Configuration scrubbing, selective TMR, and EDAC provide scalable mitigation strategies that can be tuned to mission requirements. Similarly, photonic subsystems benefit from parametric predictability. Once characterized, devices can be deployed across orbits with adjusted link margins rather than redesigned hardware. For power electronics, WBG semiconductors offer improved DD tolerance and reduced SEL susceptibility compared to Si, though voltage derating remains necessary to reduce SEB risk. Memory subsystems present a more constrained selection space. Volatile memory requires continuous scrubbing and might show retention loss in MEO, while flash exhibits potential loss of writability at high dose. Emerging NVMs provide a path toward TID-tolerant and low power storage, though control logic remains sensitive to SEEs. Mixed-signal circuits remain a vulnerability. Precision analog performance degrades monotonically under TID, while embedded digital control logic remains susceptible to transient soft errors. Design diversity can mitigate common-mode TID failures, but increased adoption of photonic sensing and conditioning may ultimately prove more effective than hardening analog electronics.

TABLE 9. Overview of dominant radiation-induced failure mechanisms for photonic components in OCT avionics across orbital regimes. Mechanisms are listed for each orbit class assuming 4 mm Al shielding. Failure severity and manifestation exhibit significant device-to-device and material-dependent variability within each technology class, particularly for COTS components where process variations, doping profiles, and integration platforms can alter radiation response by orders of magnitude. Dose-rate effects are also not accounted for.

Technology	SSO	LEO	MEO	References
Waveguides	SEE: Transient attenuation and phase shifts.	TID: Propagation loss increase, effective refractive index change, resonance wavelength shift in sensitive devices. DD: Propagation loss increase, refractive index change in sensitive devices. SEE: Transient attenuation and phase shifts.	TID: Propagation loss increase, effective refractive index change, resonance wavelength shift. DD: Propagation loss increase, refractive index change. SEE: Transient attenuation and phase shifts.	[11], [24], [28], [29], [55]–[57], [61], [62]
Modulators	SEE: Transient attenuation and phase shifts.	TID: Reduced modulation efficiency, extinction ratio degradation, effective refractive index shift, bias point shift, increased insertion loss. DD: Phase shifts, modulation efficiency reduction, attenuation. SEE: Transient attenuation and phase shifts.	TID: Reduced modulation efficiency, extinction ratio degradation, effective refractive index shift, bias point shift, increased insertion loss. DD: Phase shifts, modulation efficiency reduction, attenuation, loss of functionality in InP-based devices. SEE: Transient attenuation and phase shifts.	[63]–[68]
Amplifiers	SEE: Transient attenuation.	TID: Gain degradation, noise-figure increase, radiation-induced loss in gain medium. DD: Additional gain degradation, noise-figure increase, radiation-induced loss in gain medium. SEE: Transient attenuation.	TID: Gain degradation, noise-figure increase, radiation-induced loss in gain medium, loss of functionality. DD: Additional gain degradation, noise-figure increase, radiation-induced loss in gain medium, loss of functionality. SEE: Transient attenuation.	[69]–[71]
Lasers	SEE: Optical power transients.	TID: Small wavelength drift due to refractive index changes in passive sections. DD: Threshold current increase, slope-efficiency degradation. SEE: Optical power transients.	TID: Small wavelength drift due to refractive index changes in passive sections. DD: Threshold current increase, slope-efficiency degradation, output power reduction. SEE: Optical power transients.	[11], [72]–[76]
PDs	SEE: Transient detector current excursions.	TID: Small dark current increase in sensitive geometries. DD: Dark current increase, noise increase, responsivity change. SEE: Transient detector current excursions and bit errors.	TID: Small dark current increase, SNR degradation. DD: Dark current increase, noise increase, breakdown voltage shift, avalanche gain degradation. SEE: Transient detector current excursions and bit errors.	[61], [77]–[81]

D. ASSURANCE

The synthesis shows that conventional RHA methodologies based on pass-fail component qualification are insufficient for photonic-intensive OCTs, and increasingly inadequate for highly integrated electronic systems. Because many photonic devices remain operational while exhibiting degraded performance, qualification must emphasize parametric end-of-life behavior rather than functional survival. Effective validation requires dose- and fluence-dependent characterization of optical performance metrics, consideration of operating conditions during irradiation, and explicit translation of device-level degradation into link-level margins. For electronics, the focus must shift from universal RHA to mission-tailored mitigation strategies. SEE sensitivity varies by orders of magnitude depending on device configuration, necessitating system-level testing rather than reliance solely on component-level cross-sections. Similarly, TID and DD effects in mixed-signal and power circuits require parametric tracking rather than binary failure thresholds. System-level mitigation often proves more effective and affordable than aggressive component-level hardening. This shift requires closer integration of radiation engineering with system design, moving assurance upstream rather than treating it as a final design stage.

VI. CONCLUSION

This work presents a comprehensive radiation effects investigation for OCTs deployed across SSO, LEO, and MEO regimes, addressing a critical gap in multi-orbit RHA for heterogeneous photonic–electronic architectures. SPENVIS-based environment characterization reveals distinct radiation signatures: SSO presents a mild environment with TID below 1 krad(Si) per year and low SEE flux, LEO is dominated by proton-driven SEE with TID in the 1–10 krad(Si) per year

range, and MEO represents the most challenging regime, with TID exceeding 30 krad(Si) per year at typical Al shielding and heavy-ion fluxes driving both cumulative degradation and elevated SEE rates. Technology-level analysis reveals fundamental differences in radiation response between photonic and electronic subsystems. Photonics exhibits predominantly parametric degradation that can be bounded through margin allocation, whereas electronics remains vulnerable to discrete, stochastic failure modes that directly threaten system availability and require active mitigation. These findings motivate a progressive shift of high-speed signal-processing functions from electronics to photonics in future OCTs, reducing reliance on highly scaled, SEE-sensitive digital logic while retaining electronics for lower-speed control and monitoring tasks better suited to hardening. Reconfigurable architectures based on FPGAs, photonic subsystems with predictable degradation, WBG power semiconductors, and emerging NVMs enable component commonality across orbital regimes when coupled with environment-specific margin allocation and mitigation strategies, reducing development cost relative to fully custom designs while requiring tailored qualification for each radiation environment. Photonic devices require parametric end-of-life characterization under representative dose, fluence, and operating conditions with translation to link-level margins, while electronic systems demand mission-tailored mitigation strategies and system-level testing. Future work should focus on experimental validation of photonic devices under representative space radiation spectra, development of system-level performance models capturing correlated multi-technology degradation, long-term on-orbit data collection from operational OCTs, and standardized test protocols for photonic-intensive space systems.

REFERENCES

[1] R. C. Baumann, "Radiation-induced soft errors in advanced semiconductor technologies," *IEEE Trans. Device Mater. Rel.*, vol. 5, no. 3, pp. 305–316, Sep. 2005.

[2] J. R. Schwank, M. R. Shaneyfelt, D. M. Fleetwood, J. A. Felix, P. E. Dodd, P. Paillet, and V. Ferlet-Cavrois, "Radiation effects in MOS oxides," *IEEE Trans. Nucl. Sci.*, vol. 55, no. 4, pp. 1833–1853, Aug. 2008.

[3] J. R. Schwank, M. R. Shaneyfelt, and P. E. Dodd, "Radiation hardness assurance testing of microelectronic devices and integrated circuits: Radiation environments, physical mechanisms, and foundations for hardness assurance," *IEEE Trans. Nucl. Sci.*, vol. 60, no. 3, pp. 2074–2100, Jun. 2013.

[4] D. M. Fleetwood, "Evolution of total ionizing dose effects in MOS devices with Moore's law scaling," *IEEE Trans. Nucl. Sci.*, vol. 65, no. 8, pp. 1465–1481, Aug. 2018.

[5] J. Prinzie, F. M. Simanjuntak, P. Leroux, and T. Prodromakis, "Low-power electronic technologies for harsh radiation environments," *Nature Electron.*, vol. 4, no. 4, pp. 243–253, Apr. 2021.

[6] K. A. LaBel, A. H. Johnston, J. L. Barth, R. A. Reed, and C. E. Barnes, "Emerging radiation hardness assurance (RHA) issues: A NASA approach for space flight programs," *IEEE Trans. Nucl. Sci.*, vol. 45, no. 6, pp. 2727–2736, Dec. 1998, doi: 10.1109/23.736521.

[7] P. E. Dodd, M. R. Shaneyfelt, J. R. Schwank, and J. A. Felix, "Current and future challenges in radiation effects on CMOS electronics," *IEEE Trans. Nucl. Sci.*, vol. 57, no. 4, pp. 1747–1763, Aug. 2010.

[8] D. M. Fleetwood, "Radiation effects in a post-Moore world," *IEEE Trans. Nucl. Sci.*, vol. 68, no. 5, pp. 509–545, May 2021.

[9] G. Brunetti, G. Campiti, M. Tagliente, and C. Ciminelli, "COTS devices for space missions in LEO," *IEEE Access*, vol. 12, pp. 76478–76514, 2024.

[10] J. Dijks, S. de Jong, A. Menicucci, and I. Akay, "Systematic review of engineering and testing approaches for radiation hardness assurance in commercial space avionics," *Acta Astronautica*, vol. 238, pp. 1354–1366, Jan. 2026.

[11] G. Terrasanta, M. W. Ziarko, N. Bergamasco, M. Poot, and J. Poliak, "Photonic integrated circuits for optical satellite links: A review of the technology status and space effects," *Int. J. Satell. Commun. Netw.*, vol. 43, no. 3, pp. 210–228, Jun. 2025.

[12] D. Mao, L. Chang, H. Lee, A. W. Yu, B. A. Maruca, K. Ullah, W. H. Matthaeus, M. A. Krainak, P. Dong, and T. Gu, "Space-qualifying silicon photonic modulators and circuits," *Sci. Adv.*, vol. 10, no. 1, p. 9171, Jan. 2024.

[13] N. N. Sulaiman, N. F. Hasbullah, N. Saidin, Y. Javed, and Z. I. Khan, "Radiation-induced degradation in optoelectronic devices for satellite applications: A review," *Discover Mater.*, vol. 5, no. 1, p. 59, Mar. 2025.

[14] G. Terrasanta, A. Zinth, M. W. Ziarko, N. Bergamasco, J. Poliak, and M. Poot, "Space radiation effects on photonic integrated circuits for optical satellite payloads," *Proc. SPIE*, vol. 13530, p. 41, Jun. 2025.

[15] M. K. Gaillard, P. D. Grannis, and F. Sciulli, "The standard model of particle physics," *Rev. Mod. Phys.*, vol. 71, no. 2, pp. S96–S111, 1999.

[16] S. Weinberg, "The making of the standard model," *Eur. Phys. J. C-Particles Fields*, vol. 34, no. 1, pp. 5–13, 2004.

[17] W. N. Cottingham and D. A. Greenwood, *An Introduction to Standard Model of Particle Physics*. Cambridge, U.K.: Cambridge Univ. Press, 2023.

[18] S. Navas et al., "Review of particle physics," *Phys. Rev. D*, vol. 110, no. 3, Aug. 2024, Art. no. 030001, doi: 10.1103/PhysRevD.110.030001.

[19] R. Jung, "Radiation qualification of the cologne chip gatemate A1 FPGA," Master thesis, Fachhochschule Dortmund, Informationstechnik, CERN, p. 118, 2023.

[20] J. R. Srour, C. J. Marshall, and P. W. Marshall, "Review of displacement damage effects in silicon devices," *IEEE Trans. Nucl. Sci.*, vol. 50, no. 3, pp. 653–670, Jun. 2003.

[21] R. Ecoffet, "Overview of in-orbit radiation induced spacecraft anomalies," *IEEE Trans. Nucl. Sci.*, vol. 60, no. 3, pp. 1791–1815, Jun. 2013.

[22] T. R. Oldham and F. B. McLean, "Total ionizing dose effects in MOS oxides and devices," *IEEE Trans. Nucl. Sci.*, vol. 50, no. 3, pp. 483–499, Jun. 2003.

[23] G. N. Tzintzarov, S. G. Rao, and J. D. Cressler, "Integrated silicon photonics for enabling next-generation space systems," *Photonics*, vol. 8, no. 4, p. 131, Apr. 2021.

[24] Q. Du, "High energy radiation damage on silicon photonic devices: A review," *Opt. Mater. Exp.*, vol. 13, no. 2, p. 403, Feb. 2023.

[25] C. Han, Z. Hu, Y. Tao, E. Fu, Y. He, F. Yang, J. Qin, and X. Wang, "Proton radiation effects on high-speed silicon Mach–Zehnder modulators for space application," *Sci. China Inf. Sci.*, vol. 65, no. 12, Dec. 2022, Art. no. 222401.

[26] P. E. Dodd and L. W. Massengill, "Basic mechanisms and modeling of single-event upset in digital microelectronics," *IEEE Trans. Nucl. Sci.*, vol. 50, no. 3, pp. 583–602, Jun. 2003.

[27] G. Bruguier and J.-M. Palau, "Single particle-induced latchup," *IEEE Trans. Nucl. Sci.*, vol. 43, no. 2, pp. 522–532, Apr. 1996.

[28] P. S. Goley, Z. E. Fleetwood, and J. D. Cressler, "Potential limitations on integrated silicon photonic waveguides operating in a heavy ion environment," *IEEE Trans. Nucl. Sci.*, vol. 65, no. 1, pp. 141–148, Jan. 2018.

[29] G. N. Tzintzarov, A. Ildefonso, J. W. Teng, M. Frounchi, A. Djikeng, P. Iyengar, P. S. Goley, A. Khachatrian, J. Hales, R. Bahr, S. P. Buchner, D. Mcmorrow, and J. D. Cressler, "Optical single-event transients induced in integrated silicon-photonic waveguides by two-photon absorption," *IEEE Trans. Nucl. Sci.*, vol. 68, no. 5, pp. 785–792, May 2021.

[30] A. D. George and C. M. Wilson, "Onboard processing with hybrid and reconfigurable computing on small satellites," *Proc. IEEE*, vol. 106, no. 3, pp. 458–470, Mar. 2018.

[31] A. Johnston, "Radiation effects in advanced microelectronics technologies," *IEEE Trans. Nuclear Sci.*, vol. 45, no. 3, pp. 1339–1354, Jun. 1998, doi: 10.1109/23.685206.

[32] R. Katz, K. LaBel, J. J. Wang, B. Cronquist, R. Koga, S. Penzin, and G. Swift, "Radiation effects on current field programmable technologies," *IEEE Trans. Nucl. Sci.*, vol. 44, no. 6, pp. 1945–1956, Dec. 1997.

[33] M. Wirthlin, "High-reliability FPGA-based systems: Space, high-energy physics, and beyond," *Proc. IEEE*, vol. 103, no. 3, pp. 379–389, Mar. 2015.

[34] A. Scialdone, R. Ferraro, R. G. Alía, L. Sterpone, S. Danzeca, and A. Masi, "FPGA qualification and failure rate estimation methodology for LHC environments using benchmarks test circuits," *IEEE Trans. Nucl. Sci.*, vol. 69, no. 7, pp. 1633–1641, Jul. 2022.

[35] H. Quinn, "Radiation effects in reconfigurable FPGAs," *Semicond. Sci. Technol.*, vol. 32, no. 4, Mar. 2017, Art. no. 044001.

[36] M. J. Wirthlin, "FPGAs operating in a radiation environment: Lessons learned from FPGAs in space," *J. Instrum.*, vol. 8, no. 2, Feb. 2013, Art. no. C02020.

[37] H. Quinn, T. Fairbanks, J. L. Tripp, G. Duran, and B. Lopez, "Single-event effects in low-cost, low-power microprocessors," in *Proc. IEEE Radiat. Effects Data Workshop (REDW)*, Paris, France, Jul. 2014, pp. 1–9, doi: 10.1109/REDW.2014.7004596.

[38] A. Zimmaro, R. Ferraro, and S. Danzeca, "Radiation effects on COTS microcontrollers: Test methodology, qualification results, and mitigation strategies," in *Proc. R2EWG*, May 2025, pp. 1–23. [Online]. Available: https://indico.cern.ch/event/1542968/contributions/6504888/

[39] V. Re, L. Gaioni, M. Manghisoni, L. Ratti, V. Speziali, and G. Traversi, "Review of radiation effects leading to noise performance degradation in 100–nm scale microelectronic technologies," in *Proc. IEEE Nucl. Sci. Symp. Conf. Rec.*, Dresden, Germany, Oct. 2008, pp. 3086–3090, doi: 10.1109/NSSMIC.2008.4775008.

[40] C. J. González, C. P. Chenet, M. Budelon, R. G. Vaz, O. L. Gonçalez, and T. R. Balen, "Evaluation of a mixed-signal design diversity system under radiation effects," in *Proc. 18th IEEE Latin American Test Symp.*, vol. 9, Mar. 2017, pp. 1–6.

[41] N. N. Prokopenko, O. Dvornikov, I. V. Pakhomov, and N. Butyrlagin, "The radiation-hardened differential stages and op AMPS without classical reference current source," in *Proc. 15th RADECS*, vol. 1, 2015, pp. 1–4.

[42] J. D. Cressler, "Emerging SiGe HBT reliability issues for mixed-signal circuit applications," *IEEE Trans. Device Mater. Rel.*, vol. 4, no. 2, pp. 222–236, Jun. 2004.

[43] J. D. Cressler, "Radiation effects in SiGe technology," *IEEE Trans. Nucl. Sci.*, vol. 60, no. 3, pp. 1992–2014, Jun. 2013.

[44] R. Zuleeg and K. Lehovec, "Radiation effects in gaas junction field-effect transistors," *IEEE Trans. Nucl. Sci.*, vol. NS-27, no. 5, pp. 1343–1354, Oct. 1980, doi: 10.1109/TNS.1980.4331022.

[45] C. Miller, R. Owen, M. Rose, P. M. Rutt, J. Schaefer, and I. A. Troxel, "Trends in radiation susceptibility of commercial DRAMs for space systems," in *Proc. IEEE Aerosp. Conf.*, Mar. 2009, pp. 1–12.

[46] D. N. Nguyen, S. M. Guertin, G. M. Swift, and A. H. Johnston, "Radiation effects on advanced flash memories," *IEEE Trans. Nucl. Sci.*, vol. 46, no. 6, pp. 1744–1750, Dec. 1999.

[47] M. J. Marinella, "Radiation effects in advanced and emerging nonvolatile memories," *IEEE Trans. Nucl. Sci.*, vol. 68, no. 5, pp. 546–572, May 2021.

[48] Y. Gonzalez-Velo, H. J. Barnaby, and M. N. Kozicki, "Review of radiation effects on ReRAM devices and technology," *Semicond. Sci. Technol.*, vol. 32, no. 8, Jul. 2017, Art. no. 083002.

[49] T. Vogel et al., "Structural and electrical response of emerging memories exposed to heavy ion radiation," *ACS Nano*, vol. 16, no. 9, pp. 14463–14478, Sep. 2022.

[50] P. C. Adell and L. Z. Scheick, "Radiation effects in power systems: A review," *IEEE Trans. Nucl. Sci.*, vol. 60, no. 3, pp. 1929–1952, Jun. 2013.

[51] K. Galloway, "A brief review of heavy-ion radiation degradation and failure of silicon UMOS power transistors," *Electronics*, vol. 3, no. 4, pp. 582–593, Sep. 2014.

[52] S. J. Pearton, F. Ren, E. Patrick, M. E. Law, and A. Y. Polyakov, "Review-ionizing radiation damage effects on GaN devices," *ECS J. Solid State Sci. Technol.*, vol. 5, no. 2, p. 35, Nov. 2015.

[53] D. M. Fleetwood, E. X. Zhang, R. D. Schrimpf, and S. T. Pantelides, "Radiation effects in AlGaN/GaN HEMTs," *IEEE Trans. Nucl. Sci.*, vol. 69, no. 5, pp. 1105–1119, May 2022.

[54] C. A. Grome and W. Ji, "A brief review of single-event burnout failure mechanisms and design tolerances of silicon carbide power MOSFETs," *Electronics*, vol. 13, no. 8, p. 1414, Apr. 2024.

[55] F. Esposito, A. Stancalie, C.-D. Negut, S. Campopiano, D. Sporea, and A. Iadicicco, "Comparative investigation of gamma radiation effects on long period gratings and optical power in different optical fibers," *J. Lightw. Technol.*, vol. 37, no. 18, pp. 4560–4566, Sep. 15, 2019, doi: 10.1109/JLT.2019.2910639.

[56] Q. Du, J. Michon, B. Li, D. Kita, D. Ma, H. Zuo, S. Yu, T. Gu, A. Agarwal, M. Li, and J. Hu, "Real-time, in situ probing of gamma radiation damage with packaged integrated photonic chips," *Photon. Res.*, vol. 8, no. 2, pp. 186–193, Feb. 2020.

[57] Y. Zhou, D. Lv, D. Bi, L. Wu, R. Wang, S. Ma, E. X. Zhang, D. M. Fleetwood, and A. Wu, "Radiation-hardened silicon photonic passive devices on a 3 μm waveguide platform under gamma and proton irradiation," *Opt. Exp.*, vol. 30, no. 10, pp. 16921–16930, May 2022.

[58] Z. Ahmed, L. T. Cumberland, N. N. Klimov, I. M. Pazos, R. E. Tosh, and R. Fitzgerald, "Assessing radiation hardness of silicon photonic sensors," *Sci. Rep.*, vol. 8, no. 1, p. 13007, Aug. 2018.

[59] P. Dumon, R. Kappeler, D. J. F. Barros, I. McKenzie, D. Doyle, and R. Baets, "Measured radiation sensitivity of silica-on-silicon and silicon-on-insulator micro-photonic devices for potential space application," *Proc. SPIE*, vol. 5897, pp. 1–10, 2005.

[60] G. Brunetti, I. McKenzie, F. Dell'Olio, M. N. Armenise, and C. Ciminelli, "Measured radiation effects on InGaAsP/InP ring resonators for space applications," *Opt. Exp.*, vol. 27, no. 17, p. 24434, Aug. 2019.

[61] L. D. Ryder, R. D. Schrimpf, R. A. Reed, and S. M. Weiss, "Radiation-induced transient response mechanisms in photonic waveguides," *IEEE Trans. Nucl. Sci.*, vol. 69, no. 3, pp. 546–557, Mar. 2022.

[62] S. Girard, A. Morana, A. Ladaci, T. Robin, L. Mescia, J.-J. Bonnefois, M. Boutillier, J. Mekki, A. Paveau, B. Cadier, E. Marin, Y. Ouerdane, and A. Boukenter, "Recent advances in radiation-hardened fiber-based technologies for space applications," *J. Opt.*, vol. 20, no. 9, Aug. 2018, Art. no. 093001.

[63] S. Seif El Nasr-Storey, F. Boeuf, C. Baudot, S. Detraz, J. M. Fedeli, D. Marris-Morini, L. Olantera, G. Pezzullo, C. Sigaud, C. Soos, J. Troska, F. Vasey, L. Vivien, M. Zeiler, and M. Ziebell, "Effect of radiation on a Mach–Zehnder interferometer silicon modulator for HL-LHC data transmission applications," *IEEE Trans. Nucl. Sci.*, vol. 62, no. 1, pp. 329–335, Feb. 2015.

[64] M. Zeiler, S. S. El Nasr-Storey, S. Detraz, A. Kraxner, L. Olantera, C. Scarcella, C. Sigaud, C. Soos, J. Troska, and F. Vasey, "Radiation damage in silicon photonic Mach–Zehnder modulators and photodiodes," *IEEE Trans. Nucl. Sci.*, vol. 64, no. 11, pp. 2794–2801, Nov. 2017.

[65] M. Lalovic, C. Scarcella, A. Bulling, S. Detraz, L. Marcon, L. Olanterä, T. Prousalidi, U. Sandven, C. Sigaud, C. Soos, and J. Troska, "Ionizing radiation effects in silicon photonics modulators," *IEEE Trans. Nucl. Sci.*, vol. 69, no. 7, pp. 1521–1526, Jul. 2022.

[66] D. Gajanana, M. V. Beuzekom, M. Smit, and X. Leijtens, "Irradiation tests on InP based Mach Zehnder modulator," *J. Instrum.*, vol. 8, no. 2, Feb. 2013, Art. no. C02025.

[67] H.-C. Huang, J. I. Dadap, G. Malladi, I. Kymissis, H. Bakhru, and R. M. Osgood, "Helium-ion-induced radiation damage in $LiNbO_3$ thin-film electro-optic modulators," *Opt. Exp.*, vol. 22, no. 16, pp. 19653–19661, Aug. 2014.

[68] M. Hosseinzadeh, J. W. Teng, D. Nergui, B. L. Ringel, A. Ildefonso, A. Khachatrian, D. McMorrow, and J. D. Cressler, "Analysis of optical single-event transients in integrated silicon photonics Mach–Zehnder modulators for space-based optical communications," *IEEE Trans. Nucl. Sci.*, vol. 71, no. 4, pp. 736–743, Apr. 2024.

[69] J. Ma, M. Li, L.-Y. Tan, Y.-P. Zhou, S.-Y. Yu, and C. Che, "Space radiation effect on EDFA for inter-satellite optical communication," *Optik*, vol. 121, no. 6, pp. 535–538, Mar. 2010.

[70] R. G. Ahrens, J. Jaques, M. J. LuValle, D. J. DiGiovanni, and R. S. Windeler, "Radiation effects on optical fibers and amplifiers," *Proc. SPIE*, vol. 4285, p. 217, May 2001. [Online]. Available: https://doi.org/10.1117/12.426891

[71] M. Aubry, A. Morana, L. Mescia, J. Mekki, C. Ranger, A. Laurent, T. Robin, E. Marin, Y. Ouerdane, A. Boukenter, and S. Girard, "Combined temperature and radiation effects on the gain of Er- and Er–Yb-doped fiber amplifiers," *IEEE Trans. Nucl. Sci.*, vol. 68, no. 5, pp. 793–800, May 2021.

[72] A. H. Johnston, "Radiation effects in light-emitting and laser diodes," *IEEE Trans. Nucl. Sci.*, vol. 50, no. 3, pp. 689–703, Jun. 2003.

[73] K. Gill, R. Grabit, J. Troska, and F. Vasey, "Radiation hardness qualification of InGaAsP/InP 1310 nm lasers for the CMS tracker optical links," *IEEE Trans. Nucl. Sci.*, vol. NS-49, no. 6, pp. 2923–2929, Dec. 2002.

[74] F. Gambini, N. Andriolli, V. Nurra, M. Chiesa, F. Petroni, and S. Faralli, "Study of low-dose long-exposure gamma radiation effects on InP DBR cavity lasers from generic integration technology," in *Applications in Electronics Pervading Industry, Environment and Society*. Cham, Switzerland: Springer, 2019, pp. 77–82.

[75] A. P. Serrano, A. Soria-Gómez, D. Poudereux, J. Barbero, L. Augustin, J. M. G. Tijero, and I. Esquivias, "Evaluation of radiation hardness of InP-based photonic integrated circuits for space applications," *Proc. SPIE*, vol. 12777, Jul. 2023, Art. no. 127776F. [Online]. Available: https://doi.org/10.1117/12.2691127

[76] M. Li, J. Duan, Z. Jin, S. Pan, W. Zhan, J. Chen, J. Yu, X. Cheng, Z. Ni, C. Jin, T. K. Ng, J. Kong, X. Xu, Y. Yao, B. Xu, S. Chen, Z. Wang, and C. Zhao, "Enhanced radiation hardness of inas/gaas quantum dot lasers for space communication," *Laser Photon. Rev.*, vol. 19, no. 12, 2024, Art. no. 2500148.

[77] L. Finazzi, F. Signorelli, M. Bagatin, S. Gerardin, M. Zahidy, G. Vallone, T. Jennewein, P. Villoresi, and A. Tosi, "Radiation hardness properties and DCR reduction via laser annealing of InGaAs/InP SPADs for space applications," *Opt. Exp.*, vol. 33, no. 23, p. 47876, Nov. 2025.

[78] X. Zhou, B. White, X. Meng, S. Zhang, M. Gutierrez, M. Robbins, L. G. Rojas, N. Nelms, C. H. Tan, and J. S. Ng, "Proton radiation effect on InAs avalanche photodiodes," *Opt. Exp.*, vol. 25, no. 3, pp. 2818–2825, Feb. 2017.

[79] P. S. Goley, N. A. Dodds, M. Frounchi, G. N. Tzintzarov, R. N. Nowlin, and J. D. Cressler, "Response of waveguide-integrated germanium-on-silicon p-i-n photodiodes to neutron displacement damage," *IEEE Trans. Nucl. Sci.*, vol. 67, no. 1, pp. 296–304, Jan. 2020.

[80] P. S. Goley, G. N. Tzintzarov, S. Zeinolabedinzadeh, A. Ildefonso, K. Motoki, R. Jiang, E. X. Zhang, D. M. Fleetwood, L. Zimmermann, M. Kaynak, S. Lischke, C. Mai, and J. D. Cressler, "Total ionizing dose effects in 70-GHz bandwidth photodiodes in a SiGe integrated photonics platform," *IEEE Trans. Nucl. Sci.*, vol. 66, no. 1, pp. 125–133, Jan. 2019.

[81] G. N. Tzintzarov, J. W. Teng, A. N. Bozovich, G. R. Allen, D. Nergui, Y. A. Mensah, and J. D. Cressler, "Single-event transients in a commercially available, integrated germanium photodiode for silicon photonic systems," *IEEE Trans. Nucl. Sci.*, vol. 69, no. 3, pp. 527–533, Mar. 2022.

[82] Royal Belgian Institute for Space Aeronomy (BIRA-IASB). (2025). *Spenvis: Space Environment Information System*. [Online]. Available: http://spenvis.oma.be

[83] A. Menicucci, A. Cervone, S. Speretta, E. Bertels, and F. Topputo, "The radiation environment and effects analysis of the LUMIO mission," in *Proc. 72nd Int. Astron. Congr. (IAC)*, Oct. 2021, pp. 1–7.

[84] *ViaSat Authorization*, FCC, 2020.

[85] J. A. Van Allen, "The geomagnetically trapped corpuscular radiation," *J. Geophys. Res.*, vol. 64, no. 11, pp. 1683–1689, Nov. 1959.

[86] S. Bourdarie and M. Xapsos, "The near-Earth space radiation environment," *IEEE Trans. Nucl. Sci.*, vol. 55, no. 4, pp. 1810–1832, Aug. 2008.

[87] Y. Shprits, D. Subbotin, A. Drozdov, M. Usanova, A. Kellerman, K. Orlova, D. N. Baker, D. L. Turner, and K. Kim, "Unusual stable trapping of the ultrarelativistic electrons in the van Allen radiation belts," *Nature Phys.*, vol. 9, no. 11, pp. 699–703, Sep. 2013.

[88] P. Buehler, "Radiation belts," in *Proc. ESA Workshop Space Weather*. Noordwijk, The Netherlands: ESTEC, Nov. 1998. [Online]. Available: https://swe.ssa.esa.int/TECEES/spweather/workshops/proceedings_w1/SESSION2/buehler_radiation.pdf

[89] G. Reitz, "Characteristic of the radiation field in low Earth orbit and in deep space," *Zeitschrift Für Medizinische Physik*, vol. 18, no. 4, pp. 233–243, Dec. 2008.

[90] G. D. Badhwar, "The radiation environment in low-Earth orbit," *Radiat. Res.*, vol. 148, no. 5, p. S3, Nov. 1997.

[91] M. D. S. Pich, I. Jun, and R. W. Evans, "Empirical radiation belt models: Comparison with in situ data and implications for environment definition," *Space Weather*, vol. 15, no. 9, pp. 1165–1176, 2017.

[92] J. I. Vette, A. B. Lucero, J. A. Wright, J. H. King, J. P. Lavine, W. L. Imhof, C. O. Bostrom, D. S. Beall, J. C. Armstrong, H. H. Heckman, P. J. Lindstrom, G. H. Nakano, G. A. Paulikas, and J. B. Blake, "Models of the trapped radiation environment," NASA, Aerospace Corp. El Segundo, CA, USA, Tech. Rep. SP-3024, 1966.

[93] J. I. Vette, "The AE-8 trapped electron model environment," NASA, Aerospace Corp. El Segundo, CA, USA, Tech. Rep. TR-0200 (4230-46)-3, Nov. 1991.

[94] E. Thébault et al., "International geomagnetic reference field: The 12th generation," *Earth*, vol. 67, no. 79, pp. 1–19, 2015. [Online]. Available: https://doi.org/10.1186/s40623-015-0228-9

[95] E. Klein, M. Sznajder, and P. Seefeldt, "Proton spectra for the interplanetary space derived from different environmental models," *Frontiers Space Technol.*, vol. 3, pp. 1–13, 2022, Art. no. 933340, doi: 10.3389/frspt.2022.933340.

[96] J. Guo, B. Wang, K. Whitman, C. Plainaki, L. Zhao, H. M. Bain, C. Cohen, S. Dalla, M. Dumbovic, M. Janvier, I. Jun, J. Luhmann, O. E. Malandraki, M. Leila Mays, J. S. Rankin, L. Wang, and Y. Zheng, "Particle radiation environment in the heliosphere: Status, limitations, and recommendations," *Adv. Space Res.*, Apr. 2024. [Online]. Available: https://www.sciencedirect.com/science/article/pii/S0273117724003053

[97] R. C. Reedy, J. R. Arnold, and D. Lal, "Cosmic-ray record in solar system matter," *Science*, vol. 219, no. 4581, pp. 127–135, Jan. 1983. [Online]. Available: https://www.science.org/doi/abs/10.1126/science.219.4581.127

[98] J. R. Winckler, "Primary cosmic rays," *Radiat. Res.*, vol. 14, no. 5, p. 521, May 1961.

[99] E. N. Parker, "The passage of energetic charged particles through interplanetary space," *Planet. Space Sci.*, vol. 13, no. 1, pp. 9–49, Jan. 1965.

[100] L. J. Gleeson and I. H. Urch, "Energy losses and modulation of galactic cosmic rays," *Astrophys. Space Sci.*, vol. 11, no. 2, pp. 288–308, May 1971.

[101] E. Parizot, "Cosmic ray origin: Lessons from ultra-high-energy cosmic rays and the galactic/extragalactic transition," *Nucl. Phys. B-Proc. Supplements*, vols. 256–257, pp. 197–212, Nov./Dec. 2014. [Online]. Available: https://doi.org/10.1016/j.nuclphysbps.2014.10.023

[102] W. Liu, J. Guo, Y. Wang, and T. C. Slaba, "A comprehensive comparison of various galactic cosmic-ray models to the state-of-the-art particle and radiation measurements," *Astrophysical J. Suppl. Ser.*, vol. 271, no. 1, p. 18, Feb. 2024.

[103] C.-M. Zhang, F. Jazaeri, G. Borghello, F. Faccio, S. Mattiazzo, A. Baschirotto, and C. Enz, "Characterization and modeling of gigarad-TID-induced drain leakage current of 28-nm bulk MOSFETs," *IEEE Trans. Nucl. Sci.*, vol. 66, no. 1, pp. 38–47, Jan. 2019.

[104] P. Pourrouquet, V. Traisnel, A. Varotsou, G. Rolland, and R. Ecoffet, "Impact of the detector definition on the reverse Monte Carlo calculation results," in *Proc. 17th Eur. Conf. Radiat. Its Effects Compon. Syst. (RADECS)*, Oct. 2017, pp. 1–6.

[105] I. Sanchez Esqueda, H. J. Barnaby, and M. P. King, "Compact modeling of total ionizing dose and aging effects in MOS technologies," *IEEE Trans. Nucl. Sci.*, vol. 62, no. 4, pp. 1501–1515, Aug. 2015.

[106] Y. Iwamoto, S.-I. Meigo, and S. Hashimoto, "Estimation of reliable displacements-per-atom based on athermal-recombination-corrected model in radiation environments at nuclear fission, fusion, and accelerator facilities," *J. Nucl. Mater.*, vol. 538, Sep. 2020, Art. no. 152261.

[107] T. Nuns, C. Inguimbert, S. Soonckindt, B. Dryer, T. W. Buggey, and C. Poivey, "Experimental study of the NIEL scaling for silicon devices," in *Proc. 18th Eur. Conf. Radiat. Effects Compon. Syst. (RADECS)*, Goteborg, Sweden, Sep. 2018, pp. 1–8, doi: 10.1109/RADECS45761.2018.9328677.

JASPER DIJKS was born in The Netherlands. He received the B.Sc. degree in applied physics from Eindhoven University of Technology and the M.Sc. degree in aerospace engineering from Delft University of Technology, where he is currently pursuing the Ph.D. degree with the Space Systems Engineering Group, focusing on radiation hardness assurance of space avionics.

He is a Research and Development Engineer with the Royal Netherlands Aerospace Centre (NLR), where he focuses on embedded systems for space applications. He has contributed to multiple space-related projects in academia and industry. He also works on RISC-V-based flight processors and optical communication payloads for small satellites. His research interests include radiation hardness assurance, fault-tolerant computing, heterogeneous space avionics, and in-situ radiation monitoring for spacecraft.

SYBREN DE JONG was born in The Netherlands. He received the B.Sc. and M.Sc. degrees in space systems engineering from the Aerospace Engineering Department, Delft University of Technology. He has an educational background in electronics and space systems engineering.

With a professional career in the space sector with more than 15 years of experience, he is a Principal Research and Development Engineer with the Royal Netherlands Aerospace Centre (NLR) with a focus on space avionics systems. His research and development of control and data processing avionics for optomechanical systems applications form the key activities. His past experiences include contributions to the development and operations support for missions, such as NASA PACE, ESA Sentinel-5 precursor, Bepi-Colombo, and Solar Orbiter.

ALESSANDRA MENICUCCI received the Ph.D. degree in physics from the University of Rome Tor Vergata, in 2004, and the Laurea degree in experimental particle physics from the University of Rome La Sapienza, in 2000.

She is currently an Associate Professor with the Space Systems Engineering Department, Aerospace Engineering Faculty, Delft University of Technology. From 2006 to 2015, she was with the European Space Agency in the Space Environment and Effects Section, where she was responsible for several space radiation monitoring developments. She also supported various ESA missions in space environment and effects analysis, including Giove-B, GOCE, Alphasat, MetOp, Proba-V, EuTEF, and JUICE. She is the Program Manager of the Delfi Space Program, which aims to advance education and research through the end-to-end engineering of space missions with high relevance and impact, using very small satellites. Her previous missions include the CubeSats Delfi-C3, in 2008, and Delfi-n3Xt, in 2013, and the picosatellite Delfi-PQ, launched in January 2022. She also manages the Space Laboratory, Faculty of Aerospace Engineering, Delft University of Technology. She is the co-author of more than 60 refereed journal and conference papers. She has co-supervised three Ph.D. candidates and is supervising three more as promotor. She is also a co-investigator in several national and international projects in the field of radiation hardness assurance for miniaturized systems. Her research focuses on the development of miniaturized space systems that can be distributed onboard micro-satellites, and the analysis of the space radiation environment and its effects.

IKLIM AKAY received the B.Sc. degree in astronautical engineering from Istanbul Technical University (ITU), Istanbul, Türkiye, in 2007, the M.Sc. degree in aerospace engineering from The University of Texas at Austin, Austin, TX, USA, and the Ph.D. degree in aeronautics and astronautics from ITU, in 2020.

She is currently with the Space Systems Engineering, TU Delft, The Netherlands. During her Ph.D. studies, she conducted research on space physics and magnetotail investigations using data from the ARTEMIS probes at the NASA GSFC, USA. Additionally, she supervises thesis students on the utilization and development of model-based systems engineering (MBSE) tools. She is working on the NEXTGEN DASE project, which focuses on the development of educational lines to implement the Dutch approach to systems engineering. She is actively involved in the university's educational research on graduating "Future-ready Engineering" students and the teaching curriculum, specifically lecturing for the aerospace design and systems engineering elements, the design synthesis exercise, and supervising detailed design projects. Her research interests bridge space physics and engineering, focusing on applying data science and machine learning models to tackle scientific challenges from an engineering perspective, particularly in magnetopause investigation, radiation analysis, and space situational awareness.

NIELS DONKERS was born in The Netherlands. He received the B.Eng. degree in electronics from Utrecht University of Applied Sciences.

He is currently an Electronics Architect with FSO Instruments, where his main focus areas are requirements definition, architectural design, and industrialization of optical communication terminals for use in satellites, high-altitude pseudo satellites, and airborne applications. He has a broad interest in topics, such as radiation hardness assurance, fault analysis and mitigation, design for test and manufacturing, and automated production technologies. He has since expanded his knowledge on electronics, working as an electronics designer and researcher for functional safety and explosion safety systems, electronic warfare, software-defined radio, phased arrays, and laser communication systems.